



**STUDY OF THE METHODS FOR MODELLING INCOMPLETE ASSEMBLIES  
IN POOLS FOR CRITICALITY CALCULATIONS**

Lappeenranta–Lahti University of Technology LUT

Master's Programme in Nuclear Engineering, Master's thesis

Safe and Reliable Nuclear Applications (SARENA) Erasmus Mundus,

Nuclear Reactors Operation and Safety (NROS) track

2024

Paula Sánchez Agostini

Examiners: Juhani Hyvärinen, Tanja Goričanec

Instructors: Matthieu Duluc, Laura Faure-geors, Ville Rintala

## ABSTRACT

Lappeenranta–Lahti University of Technology LUT

LUT School of Energy Systems

Energy Technology

Paula Sánchez Agostini

### **Study of the methods for modelling incomplete assemblies in pools for criticality calculations**

Master's thesis

2024

79 pages, 67 figures, 3 tables and 2 appendices

Examiners: Juhani Hyvärinen, Tanja Goričanec

Keywords: Criticality safety, Missing Fuel Rods, Metropolis-Hastings algorithm.

#### Abstract

The presents work focuses on the methods to evaluate the criticality of incomplete assemblies; where the absence of an unknown number of fuel rods (the so-called “Missing Fuel Rods”) can lead to an increase in reactivity in the spent fuel storage pool.

Different methods to model the effect of the Missing Fuel Rods spatial distribution on criticality have been proposed in the last years. The aim of this work is to study and implement the so-called “contact surface method”, and to compare it with the method of generational Genetics Algorithms. The contact surface, a geometric parameter of the Missing Fuel Rods pattern, should be able to parametrize the reactivity of the assembly.

The method has been applied to several study cases of a PWR assembly. Three environments have been studied: the isolated assembly, the assembly surrounded by two sides of water and two sides of concrete, and the array of assemblies. To evaluate the method, the Metropolis-Hastings algorithm has been put in place to create the configurations of interest. For the criticality calculations, the Monte Carlo code SERPENT2 has been used.

Results proved that the contact surface parameter gathers together configurations with similar  $k_{\text{eff}}$ , with more or less precision for the different study cases. Some of the patterns generated by means of Metropolis-Hastings algorithm have been found to be more reactive than patterns obtained by other methods, such as the generational Genetics Algorithms. This gives further evidence of the pertinence of the method.

## ACKNOWLEDGEMENTS

I am grateful to my examiners, Juhani Hyvärinen from LUT University and Tanja Goričanec from the University of Ljubljana (UL), for their valuable feedback. I would like to express my deep gratitude to my supervisors at Framatome, Matthieu Duluc and Laura Faure-geors, for their invaluable help and support, their availability, and their insightful advice and guidance. My sincere thanks also go to Ville Rintala from LUT University for his attention and for reading my work with great care, providing precise and thoughtful comments. I would also like to offer my sincere thanks to all the instructors who taught me throughout the SARENA Master's program—at IMT in Nantes, LUT in Lappeenranta, and UL in Ljubljana—for both their academic and personal support.

To the SARENA Master program, I extend my appreciation for providing me with such an enriching experience through the Erasmus Mundus program and for the opportunity to be educated in the fascinating field of nuclear engineering. I am also deeply thankful to Framatome for allowing me to undertake this internship within such a renowned company. My gratitude goes especially to the Neutron, Radiation Protection, and Criticality section of Framatome Lyon for their warm and sincere welcome.

To my friends in Colegio Mayor San Juan de Ribera and the institution itself: without you, I would not be who I am today. Lastly, to my family, especially to my Abueli.

## SYMBOLS AND ABBREVIATIONS

$n$	number of MFR	
$k_{\text{eff}}$	effective multiplication factor	
$k_{\infty}$	infinite multiplication factor	
$s$	normalised contact surface	
$V_{\text{mod}}$	volume of moderator material	$\text{cm}^3$
$V_{\text{fiss}}$	volume of fissile material	$\text{cm}^3$
$s_{\text{target}}$	target normalised contact surface in the MH algorithm	
$\pi$	target distribution in the MH algorithm	
$Q$	transition kernel in the MH algorithm	
$A$	acceptance ratio in the MH algorithm	
$\sigma$	microscopic cross section	$\text{b}$
$\Sigma$	macroscopic cross section	$\text{cm}^{-1}$
$\Phi$	neutron flux	$(\text{cm}^2 \cdot \text{s})^{-1}$
$\eta$	thermal fission factor	
$\varepsilon$	fast fission factor	
$p$	resonance escape probability	
$f$	thermal utilization factor	
$\mathbf{F}$	fission matrix	

## Abbreviations

CEA	French Atomic Energy Commission
gGA	Generational Genetic Algorithm
IRSN	French Institute for Radiation Protection and Nuclear Safety
JEFF	Joint Evaluated Fission and Fusion
MCMC	Markov chain Monte Carlo
MFR	Missing Fuel Rods
MH	Metropolis-Hastings
PWR	Pressurised Water Reactor

## Table of contents

Abstract

Acknowledgements

Symbols and abbreviations

1	Introduction: Incomplete Assemblies in Nuclear Criticality Safety.....	13
1.1	Incomplete Assemblies: What Are They and Where Can They Be found? .....	13
1.2	Modelling Incomplete Assemblies: How to Find the Most Reactive Patterns ....	15
2	Theoretical Notions: From the Basics of Criticality and Neutronics to Existing Knowledge of Incomplete Assemblies .....	17
2.1	Back to Criticality and Neutronics.....	17
2.2	Overview of the Missing Fuel Rod Problem: Why Is It a Challenge For Criticality Safety	22
2.3	Calculation Codes .....	25
2.4	Review of Literature: Approaches to Treat Incomplete Assemblies in Criticality Safety – Description of the Contact Surface Method.....	26
2.5	Metropolis-Hastings Algorithm: A Useful Tool for the Contact Surface Method	34
3	Methodology: Modelling Incomplete Assemblies and Application of the Contact Surface .....	36
3.1	Methods For the Generation of Configurations: How to Create the Patterns.....	36
3.2	Criticality Calculations: How to Evaluate $k_{\text{eff}}$ of the Generated Configurations.	39
3.3	Python Programming: Task Automation .....	39
3.4	Study Cases: Parameters of the Generated Configurations .....	41
3.5	Some Useful Tools to Refine the Contact Surface Parameter .....	48
4	Results of Modelled Configurations and Their Relation to the Contact Surface .....	53
4.1	The Isolated Assembly: Application and Validation of the Contact Surface Method	54
4.2	Other Boundary Conditions: Is the Contact Surface Method Still Valid?.....	58

4.3	Comparison of Most Reactive Patterns: Contact Surface Method vs. Generational Genetic Algorithm.....	63
4.4	Attempts to Refine the Contact Surface Parameter: Results .....	66
5	Conclusions .....	76
	References.....	77

## Appendix

Appendix 1.	Study cases. ....	1
Appendix 2.	Results of the array for different distances between assemblies.....	2

## Figures

Figure 1. Scheme of a 17×17 incomplete assembly with 9 MFR.....	14
Figure 2. Fission chain reaction.....	17
Figure 3. Fission cross section for 92235U. Source: JANIS web (JEFF 3.1.1 library). ....	19
Figure 4. Capture cross section for 92238U. Source: JANIS web (JEFF 3.1.1 library). ....	19
Figure 5. Energy spectrum of neutrons from fission. Source: JANIS web. ....	20
Figure 6. Scheme of $k_{\text{eff}}$ as a function of the number of MFR.....	23
Figure 7. $k_{\text{eff}}$ as a function of the number of MFRs for an isolated assembly. For a given number of MFRs, around 40 geometrical configurations are calculated. Source: Dechenaux et al. 2023.....	24
Figure 8. Example of two equivalent configurations (A transformed in B by rotation of 90°).....	25
Figure 9. Scheme of the CRISTAL procedure for the homogenisation method. ....	28
Figure 10. A pattern of 25 MFR in a 17×17 assembly. ....	28
Figure 11. Two-zone model of the homogenised fuel assembly. ....	29
Figure 12. A pattern of 35 MFR in a 17×17 assembly. ....	29
Figure 13. Incomplete assembly (left) and its corresponding chromosome (right).....	30
Figure 14. Most penalising pattern in a 16×16 assembly found by CEA with gGA. ....	31
Figure 15. Incomplete assembly (left) and its interpretation as random binary mixture (right). ....	32
Figure 16. Example of the calculation of $S$ : +1 for each edge in the frontier between the two materials. $S = 14$ in the example. ....	32
Figure 17. Binary mixture representing an assembly where $s < 0$ . For the example: $S=16$ , $S_{\text{border}}=24$ , $n=20$ , $s = -0.1$ .....	33
Figure 18. Histogram of the distribution of the contact surface for a sample of 106 randomly generated configurations, with $n = 80$ in the 17×17 assembly.....	37
Figure 19. Distribution of the configurations in the $(n, s)$ space. For each number of MFR, 1000 random configurations were generated.....	38
Figure 20. Schematic representation of the methodology. ....	40
Figure 21. $k_{\text{eff}}$ as a function of $s$ for 4 MFR in the 5×5 isolated assembly. ....	42
Figure 22. 2D histogram of the distribution of the configurations for the isolated 5×5 assembly, no MFR in periphery.....	43
Figure 23. 5×5 configurations with MFR in periphery, along with their values of $s$ . ....	43
Figure 24. Distribution in the $(n, s)$ space of the 1470 configurations randomly generated. ....	44
Figure 25. Schemes of the water-concrete boundary conditions. Non-proportional dimensions in the drawing. ....	46
Figure 26. Study case 2: Isolated 16×16 assembly with 20 fixed guide tubes. ....	47
Figure 27. Most penalising pattern CEA, for study case 2. Source: CEA, 2023.....	47
Figure 28. Partition of the assembly in rings for the spatial detectors.....	50
Figure 29. Three configurations of study case 6 used for the fission matrix. They all presented $n = 12$ MFR and $s = 1$ . The red circles represent the 12 MFR. ....	51
Figure 30. Regions of the assembly defining the partitions for the fission matrix.....	51
Figure 31. Two 17×17 incomplete assemblies with 50 MFR, immersed in water, and their respective multiplication factors. Surrounding water thickness truncated in the scheme. ...	53

Figure 32. Results of $k_{\text{eff}}$ for an isolated $17 \times 17$ assembly as a function of $n$ . For each $n$ , 50 configurations have been sampled. ....	54
Figure 33. $k_{\text{eff}}$ for the $5 \times 5$ isolated configurations. ....	55
Figure 34. $k_{\text{eff}}$ for the $17 \times 17$ isolated assembly, random generation (1470 cases). ....	56
Figure 35. $k_{\text{eff}}$ results for the $17 \times 17$ isolated assembly, MH generation. ....	56
Figure 36. $k_{\text{eff}}$ results for the $17 \times 17$ isolated assembly. MH generation, $s=0.6$ , $s=0.8$ , $s=1.57$	
Figure 37. Dispersion of the samples in the $(n, s)$ space, $17 \times 17$ isolated assembly. ....	57
Figure 38. $k_{\text{eff}}$ for the $5 \times 5$ assembly with no MFR in periphery, water-concrete. ....	58
Figure 39. $k_{\text{eff}}$ results for the $17 \times 17$ assembly, water-concrete. MH generation, $s=0.6$ , $s=0.8$ , $s=1$ . ....	59
Figure 40. Dispersion of the samples in the $(n, s)$ space. Comparison of isolated and water water-concrete concrete conditions ( $17 \times 17$ assembly). ....	59
Figure 41. $k_{\text{eff}}$ as a function of contact surface for the different distances between assemblies. ....	60
Figure 42. Dispersion of $k_{\text{eff}}$ for the differences distance in the array of assemblies. ....	61
Figure 43. Standard deviation as a function of the distance (in terms of pitch), $n=40$ , $s=0.6$ . .....	61
Figure 44. $k_{\text{eff}}$ as a function of $n$ and $s$ for the array of assemblies, distance= $5 \times$ pitch. ....	62
Figure 45. Dispersion of the samples in the $(n, s)$ space, array of assemblies with distance = $5 \times$ pitch. ....	62
Figure 46. $k_{\text{eff}}$ for the $16 \times 16$ assembly, comparison MH generation and CEA result. ....	63
Figure 47. $k_{\text{eff}}$ for the $16 \times 16$ assembly, comparison MH generation for $s$ around $s_{\text{CEA}}$ and CEA result. ....	64
Figure 48. Histogram of $k_{\text{eff}}$ for 500 configurations generated by MH with no MFR in periphery, $n=50$ , $s=s_{\text{CEA}}$ . ....	65
Figure 49. Four factors for $n=20$ . ....	67
Figure 50. Four factors for $n=100$ . ....	68
Figure 51. Standard deviation of each factor in the $n$ - $s$ space, compared to the standard deviation of $k_{\text{eff}}$ . ....	69
Figure 52. Four-factor formula results for the study case 6. ....	69
Figure 53. Reaction rates in the three configurations in Table 3. ....	70
Figure 54. Ratios of magnitudes from detectors for the configurations in Table 3. ....	70
Figure 55. Flux by ring in the assembly for the configurations in Table 3. ....	71
Figure 56. Reaction rates by ring in the assembly for the configurations in Table 3. ....	71
Figure 57. Ratios of magnitudes from detectors, configurations of study case 6 with different values of $s$ . ....	72
Figure 58. Elastic scattering and capture rates by energy of the neutron in water within the assembly. ....	73
Figure 59. Fission matrix of the inner, medium and outer configurations. ....	73
Figure 60. $k_{\text{eff}}$ as a function of $\sigma_s$ , results for the array of assemblies, distance = $5 \times$ pitch, $n=80$ , $s=0.4$ (50 configurations). ....	74
Figure 61. $k_{\text{eff}}$ as a function of $\sigma_s$ , results for the array of assemblies, distance = $5 \times$ pitch. ....	75
Figure 62. $k_{\text{eff}}$ as a function of $\sigma_s$ in the isolated $17 \times 17$ assembly. ....	75
Figure 63. Scheme of the $17 \times 17$ isolated assembly. For a better visualisation, water thickness is the picture is not scaled to its value. ....	1

Figure 64. Example of two $5 \times 5$ configurations that are no longer neutronically equivalent after the change in the environment.....	1
Figure 65. Scheme of the periodic boundary conditions applied to the assembly to simulate an array of assemblies.....	1
Figure 66. $k_{\text{eff}}$ as a function of $s$ .....	2
Figure 67. $k_{\text{eff}}$ as a function of $s$ for the isolated case.....	2

## Tables

Table 1. Number of unique possible configurations for a given number of MFR in the $17 \times 17$ assembly ( $N=289$ ). Equivalent configurations by symmetry and rotation have been removed. ....	25
Table 2. Synthesis of the different study cases.....	41
Table 3. Patterns of the configurations of the $16 \times 16$ assembly to study in detail.....	64

# 1 Introduction: Incomplete Assemblies in Nuclear Criticality Safety

Safety is of paramount importance in the nuclear industry, with criticality management being one of its key axes. Nuclear criticality safety involves maintaining subcriticality during handling of fissile material, to prevent an uncontrolled, self-sustained nuclear chain reaction which might cause health risk for humans and economical damages through the release of radiation or energy. Criticality safety assessments are required at various stages of the nuclear fuel cycle, including enrichment processes, manufacturing of nuclear fuel, fuel transportation, fresh fuel storage, fuel pool, loading operations, spent fuel storage facilities and final disposal. Given the importance of this work, these kinds of studies aim at meticulous exploring all potential scenarios and effectively identifying the most penalising ones.

The handling of fissile material includes the presence of incomplete assemblies in the spent fuel pools. An incomplete assembly is one in which an arbitrary number of fuel rods have been removed from random locations, typically due to damage from irradiation and mechanical stresses in the reactor core. The locations in the assembly where a fuel pin is absent are the so-called “Missing Fuel Rods” (hereafter referred as MFR).

The presence of MFR in the assembly can lead to an increase in its reactivity. The last investigations prove the impact of the spatial distribution of the MFR on reactivity, so the criticality assessment of incomplete assemblies in the (spent) fuel pool should consider such spatial distribution to find the most penalising cases.

In this section, the definition, causes and consequences of the incomplete assemblies’ phenomenon are presented, as well as the importance and challenges it poses from the criticality safety perspective.

## 1.1 Incomplete Assemblies: What Are They and Where Can They Be found?

An incomplete assembly is an assembly where an arbitrary number of fuel pins are removed at random locations ([Dechenaux et al. 2023](#)). Consequently, the locations in the assembly

are occupied by either fuel pins, guide tubes<sup>1</sup>, or, where a fuel pin is absent, by the so-called “Missing Fuel Rods” (MFR). An example is illustrated in Figure 1.

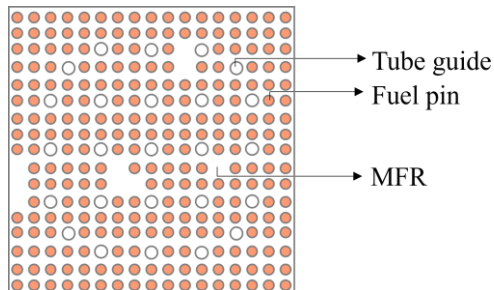


Figure 1. Scheme of a 17×17 incomplete assembly with 9 MFR.

Different causes can lead to incomplete assemblies, both during their manufacturing process and throughout their life cycle. On the one hand, during the manufacture of the assembly, configurations with MFR might be encountered during the filling and possible removal of the rods within the fuel assembly in normal or abnormal conditions. On the other hand, due to irradiation and mechanical stresses in the reactor core, fuel rods may become damaged, for instance due to the break of the cladding, and need to be removed and replaced by aluminium or steel tubes. These tubes are not considered in the criticality-safety demonstrations due to their capacity as absorbents. Therefore, we can talk about incomplete assemblies being found at the spent fuel pool in the fuel building, at the transport packaging and at the storage stage. Both the loading and unloading of the transport packaging are unitarily done, so that the assembly is isolated; while during the transport itself, in the spent fuel pool at the fuel building and at the reprocessing plant, the interaction between assemblies must be studied.

In all the described situations, as with any operation involving assemblies, criticality-safety studies must ensure that there is no risk of reaching criticality. Indeed, the presence of missing fuel rods (MFR) impacts the criticality of assemblies. When immersed in a moderation media, like water in the case of the (spent) fuel storage pool, an incomplete assembly may experience an increase in reactivity. This is because the complete PWR

---

<sup>1</sup> Guide tubes are vacant tubes in the assembly for control rods or in-core instrumentation. Due to the minimal impact of the tube material on reactivity, they have a similar effect to MFR and can be virtually treated as such. The difference between guide tubes and MFR is that guide tubes are located in fixed, known positions. In research on modelling MFR, some studies ([Dechenaux et al. 2023](#)) remain as general as possible and examine hypothetical assemblies without guide tubes, while other ([Dupas, 2023](#)) include the specific positions of guide tubes in the assembly being studied.

assembly is designed to be under-moderated, so the presence of water in the form of MFR increases reactivity compared to the complete assembly.

## 1.2 Modelling Incomplete Assemblies: How to Find the Most Reactive Patterns

Several studies have proved that the specific positions of the MFR within the incomplete assembly have an effect on its reactivity ([Albert et al. 2019](#), [Dechenaux et al. 2023](#)). Yet, the number of possible MFR patterns is far too large to find the most reactive pattern via explicit criticality calculations for different fuel rod patterns ([Hoefler, 2019](#)).

In this context, some methods are being developed to circumvent the problem of the enormous number of possible configurations to study, while preserving the rigour needed in a criticality-safety analysis. The methods rely on the possibility to find the most penalizing cases without doing all possibilities. Two approaches stand out:

- Optimization algorithms, by coupling the pattern generation with the criticality calculations ([Dupas, 2023](#)), such as Generational Genetic Algorithms (gGA),
- Introduction of a new parameter complementary to  $n$ , capable of gathering different configurations, that would be “neutronically equivalent” so would have reasonably similar values of  $k_{\text{eff}}$ . The present work focuses on the parameter proposed by the French Institute for Radiation Protection and Nuclear Safety (IRSN), the so-called “contact surface”  $s$  ([Dechenaux et al. 2023](#)).

This work aims at the implementation of the contact surface method and posterior comparison of its results to the gGA’s results. It focuses on the criticality of the incomplete assembly at the storage level, immersed in water and with no constraint on the number of the MFR. Some further studies of the neutronic behaviour of the configurations of incomplete assemblies, for instance with the use of fission matrix, are also done to complement the contact surface method.

The mission consists in:

- Adoption of the contact surface method and the associated tools. The method was first applied to isolated assemblies (a single assembly surrounded by water with no interaction with other assemblies), for which it was originally developed,

- Application of the method to new cases where the conditions of the isolated assembly were changed. In particular:
  - Assembly surrounded by two sides of water and two sides of concrete. It is a pertinent configuration from the industrial point of view since it could happen if the assembly was in a corner of the (spent) fuel storage pool,
  - Array of assemblies, of interest since it represents the situation of a real storage,
- Comparison of the results from the surface method with the results from Generational Genetic Algorithms (gGA) done by the French Atomic Energy Commission (CEA),
- Improvement of the contact surface  $s$  parameter. Based on the results obtained in the previous missions, further analyses were conducted to address the limitations of the contact surface method.

The study was conducted during an internship within the Neutron, Radiation Protection, and Criticality section of the Technical and Engineering Department at Framatome. Framatome expressed a strong interest in this topic, as it represents one of the most emergent challenges in the criticality field. Currently, Framatome performs criticality assessments of incomplete assemblies using an oversimplified approach. As part of their commitment to advancing research and innovation, the company aims to contribute to the development and implementation of a more accurate and robust method.

Theoretical notions and literature about how to model the spatial distribution will be reviewed in section 2 with the implementation of the contact surface method explained in section 2.4.4 . The methodology of the work will be presented in section 3 . In 3.1 the Metropolis-Hastings algorithm and its application to the generation of incomplete assemblies configurations will be described. The criticality calculations of these configurations will be done with SERPENT, and will be detailed in 3.2 . The last part of the methodology, 3.4 will present the study cases of the research: the different type of assemblies studied and their boundary conditions.

The results of  $k_{\text{eff}}$  for the different study cases will be presented and related to the contact surface parameter in sections 4.1 and 4.2 . Section 4.3 will compare these results with the gGA's results. Finally, in section 4.4 outputs from other tools used in SERPENT, like neutron detectors and fission matrix, will be presented.

## 2 Theoretical Notions: From the Basics of Criticality and Neutronics to Existing Knowledge of Incomplete Assemblies

The theoretical basis supporting this work go from the more general notions of criticality and neutronics, to the revision of the methods to treat the incomplete assembly problem, and ultimately to the specific techniques for the generation of the spatial distributions of the assemblies.

### 2.1 Back to Criticality and Neutronics

#### 2.1.1 The Fission Chain Reaction

In a neutron induced fission reaction, the incident neutron causes the fission of a heavy nuclei into two smaller nuclei, called fission fragments. The fission also results in the production of gamma radiation and 2 or 3 new neutrons. These resulting neutrons may cause new fissions in what is called the fission chain reaction, illustrated in Figure 2.

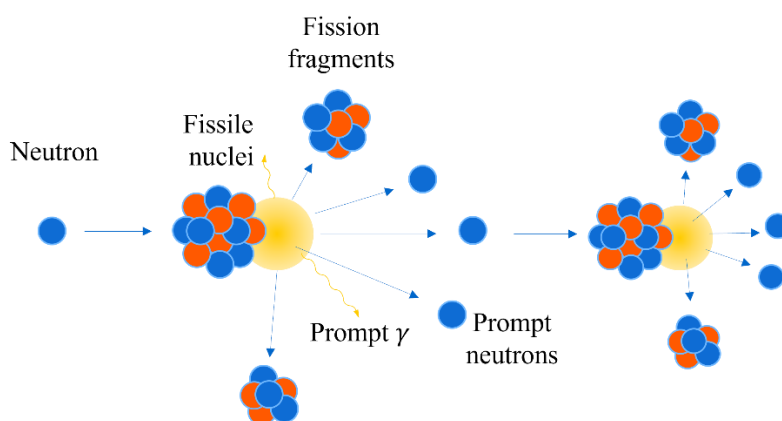


Figure 2. Fission chain reaction.

The effective neutron multiplication factor  $k_{\text{eff}}$  describes the evolution of this phenomenon. It is defined as the average ratio between the neutron population of two successive generations.

$$k_{\text{eff}} = \frac{N_{i+1}}{N_i} \quad (1)$$

To have a self-sustained nuclear chain reaction,  $k_{\text{eff}}$  must be equal to 1: the system is critical, and the neutron population remains stable over time. If  $k_{\text{eff}} < 1$ , neutron population dies out and the system is said to be subcritical, while  $k_{\text{eff}} > 1$  implies a supercritical state with an exponentially increasing neutron population.  $k_{\text{eff}}$  is a dimensionless magnitude but differences in values of  $k_{\text{eff}}$ , margins and errors are commonly expressed in the "non-SI" unit pcm, representing *per cent mille* or  $10^{-5}$  ([Reuss, 2009](#)).

During handling (transport, storage and any other manipulation) of fissile material outside the reactor, the criticality-safety analyses must guarantee  $k_{\text{eff}} < 1$  within a certain margin. In France, the general rule is  $k_{\text{eff}} + 3\sigma \leq 0,95$  in normal conditions and  $k_{\text{eff}} + 3\sigma \leq 0,97$  during an accident ([Autorité de sûreté nucléaire \(ASN\), 1984](#)).

The effective neutron multiplication factor results from the balance of the different mechanisms that contribute (either by appearance or loss of neutrons) to the neutron flux  $\Phi(\vec{r}, E, \vec{\Omega}, t)$ , proportional to the density of neutrons with energy  $E$  and direction  $\vec{\Omega}$ , at a certain time  $t$  in position  $\vec{r}$ . Indeed, apart from the production of neutrons by the reaction of fission, neutrons can experience other reactions with the nuclei, like absorption, that results in their lost.

To describe the number of reactions between the neutron flux  $\Phi$  and the target nuclei, the concept of cross-section is used. Microscopic cross sections  $\sigma$  represent indeed the probability of an interaction between the neutron and the target. Experimentally obtained, cross sections are specific to each target nuclei and type of reaction and are dependent on the energy of the incident neutron. They are commonly expressed in barn ( $1 \text{ b} = 10^{-24} \text{ cm}^2$ ). Figure 3 and Figure 4 show fission cross section for  $^{235}_{92}\text{U}$  and radiative capture cross section for  $^{238}_{92}\text{U}$ . The great dependence of the cross sections with the energy of the incident neutron can be perceived.

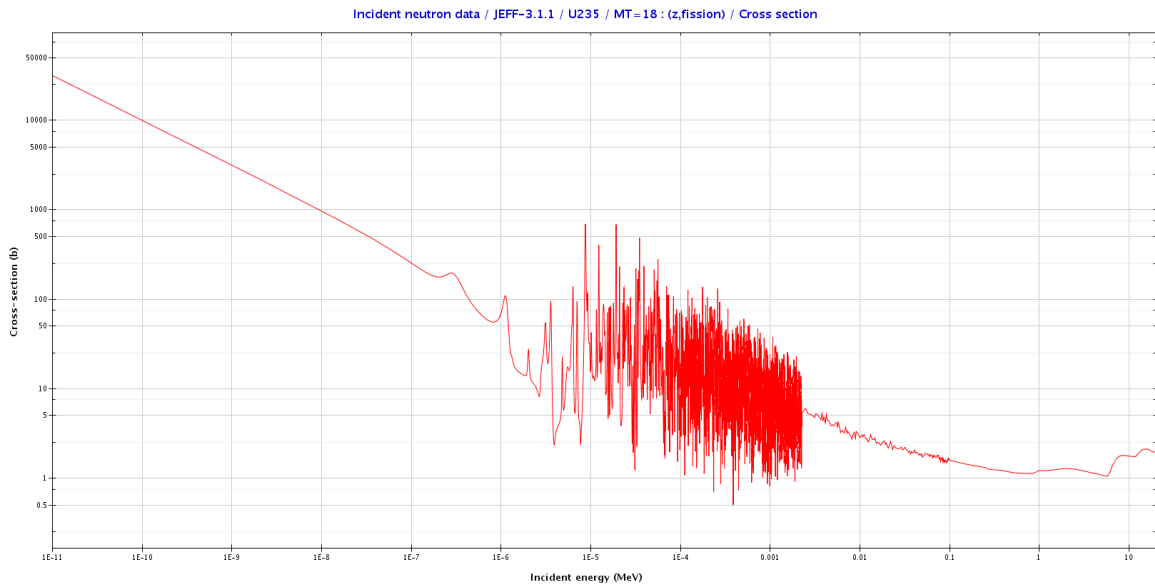


Figure 3. Fission cross section for  $^{235}_{92}\text{U}$ . Source: [JANIS web](#) (JEFF 3.1.1 library).

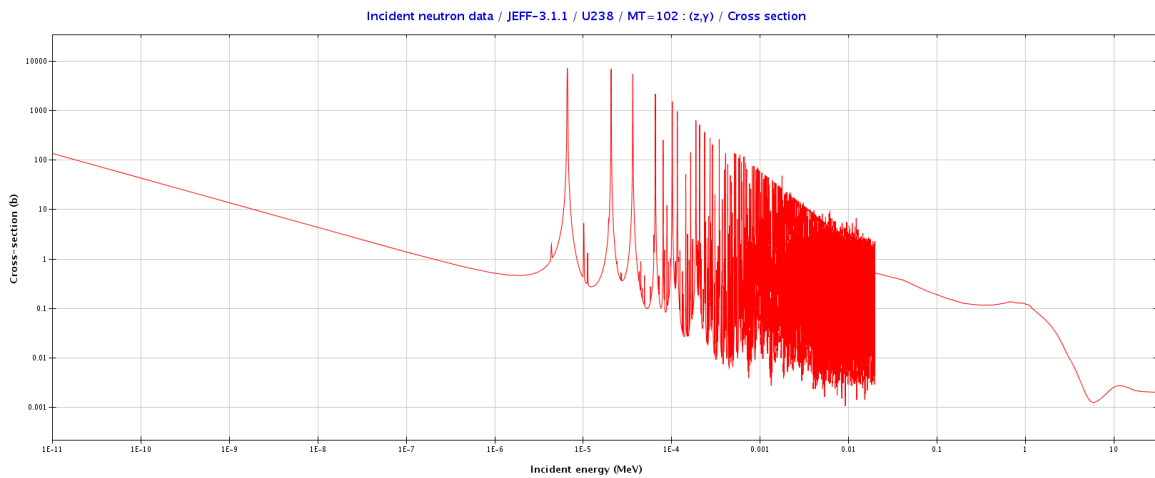


Figure 4. Capture cross section for  $^{238}_{92}\text{U}$ . Source: [JANIS web](#) (JEFF 3.1.1 library).

While microscopic cross sections are characteristic of the interaction with the individual target, to describe the interaction with a material containing a big amount of target nuclei, macroscopic cross sections  $\Sigma = \sigma N$ , where  $N$  is the volumetric density of nuclei in the material, are introduced ([Henry, 1975](#)).

The utility of macroscopic cross sections is that it allows the easy calculation of the reaction rate  $R$  as

$$R(\vec{r}, E, \vec{\Omega}, t) = \Sigma \Phi(\vec{r}, E, \vec{\Omega}, t) \quad (1)$$

From Figure 3 it can be deduced that it is more convenient to aim at fission reactions with  $^{235}\text{U}$  in the low energy range. However, the energy spectrum of neutrons from fission of  $^{235}\text{U}$  is shifted to higher energies (Figure 5); neutrons are in average born with 2 MeV of energy.

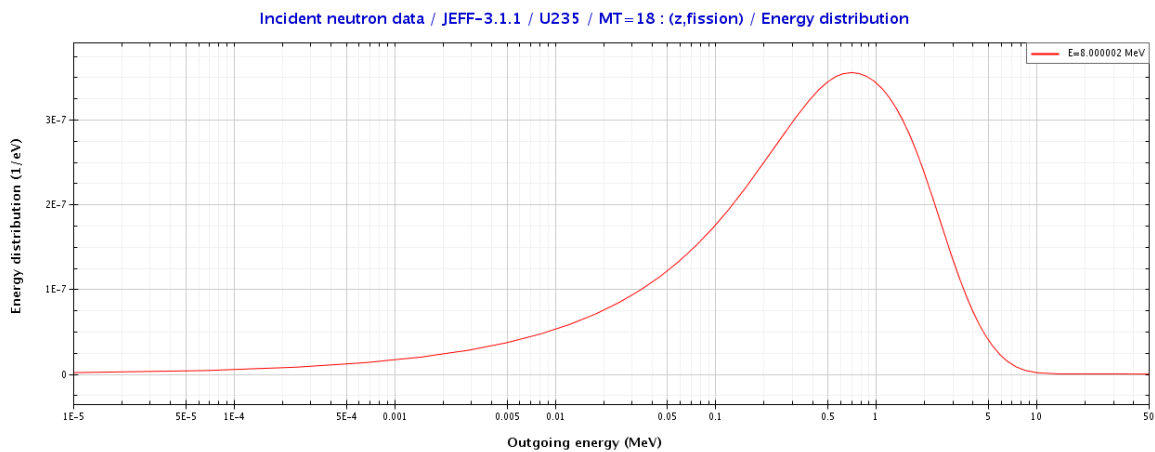


Figure 5. Energy spectrum of neutrons from fission. Source: [JANIS web](#).

This explains the need to slowdown neutrons from their initial energy to energies in the thermal range throughout what is called “moderation”. The process is mainly carried out by successive elastic scatterings of the neutrons with light nuclei, which maximise the amount of energy lost per collision ([Duderstad, 1977](#)). Hydrogen in water (also used as coolant) serves as the primary moderator material in PWR reactors.

### 2.1.2 Six-Factor Formula

The effective multiplication factor can be defined in terms of the physical process that neutrons experience. This way, it can be expressed as a product of six factors that represent the cycle of the neutrons in the system.

Let's first describe the system for an infinite medium (without leakage). The multiplication factor  $k_\infty$  is defined by the four-factor formula

$$k_\infty = \eta \epsilon p f \quad (2)$$

where:

- $\eta$  is the thermal fission factor,
- $\epsilon$  is the fast fission factor,
- $p$  is the resonance escape probability,
- $f$  is the thermal utilization factor.

The thermal fission factor  $\eta$  is the ratio of total neutrons produced from fission to the neutrons absorbed by the fissile material, so it can be expressed as

$$\eta = \frac{\nu \sigma_f^F}{\sigma_a^F} \quad (3)$$

where  $\nu$  is the average number of neutrons produced per fission, and  $\sigma_f^F$  and  $\sigma_a^F$  are respectively the microscopic fission and absorption cross sections for the fissile material.

The other three factors can be seen as corrections to  $\eta$ . The fast fission factor  $\epsilon$  accounts for the additional fissions provoked by fast neutrons. It is defined as the ratio of all neutrons from fission to the fission neutrons from only thermal neutrons. It is not odd then that this factor falls within the range [1.0, 1.3] ([Duderstadt, 1977](#)). The resonance escape correction  $p$  accounts for all the neutrons produced from fission that neither produce fast fissions nor reach the thermal region since they get absorbed in the process. It is defined as the ratio of fission neutrons slowed to thermal energies without absorption, to the total fission neutrons, so  $p < 1$  in all cases. The thermal utilization  $f$  correction considers the fact that the already *thermal* neutrons may not be absorbed by the fissile material, but by other media. It is the ratio of neutrons absorbed by the fuel isotope to the neutrons absorbed anywhere.

In a non-infinite medium, two factors are added to account for the leakages:

- Fast non-leakage probability  $P_f$ ,
- Thermal non-leakage probability  $P_{th}$ .

So that the six-factor formula for the effective multiplication factor  $k_{\text{eff}}$  is

$$k_{\text{eff}} = k_{\infty} P_f P_{th} = \eta \epsilon p f P_f P_{th} \quad (4)$$

### 2.1.3 Fission Matrix

Fission matrix  $\mathbf{F}$  is an optional output from Monte-Carlo simulations. In a system divided into multiple cells, the  $F_{ij}$  coefficient represents the number of neutrons born in the  $i$  cell from fissions induced by neutrons that were born in the  $j$  partition. For example, fission matrix capabilities have been incorporated into the MCNP Monte Carlo code. Using this functionality, the fission matrix has been computed for 2D and 3D whole-core PWRs, allowing the calculation of higher eigenvalues and eigenfunctions of the fission neutron source distribution from the matrix ([Carney et al., 2013](#)).

By definition, the spatial interactions within the system are encoded in the elements of the fission matrix, which makes it an interesting tool to analyze the effect of the location of MFR in an assembly.

## 2.2 Overview of the Missing Fuel Rod Problem: Why Is It a Challenge For Criticality Safety

The capacity of neutrons to reach thermal energies affects the neutron multiplication factor. The efficiency of the moderation is usually described by the moderation ratio: the ratio between the moderation volume and the fissile material volume  $\frac{V_{mod}}{V_{fiss}}$ . The presence of the moderator allows the slowing down of neutrons and leads to higher values of  $k_{\text{eff}}$ . An optimum value of  $\frac{V_{mod}}{V_{fiss}}$  exists, for which  $k_{\text{eff}}^{\text{max}}$  is found. Afterwards,  $k_{\text{eff}}$  decreases with  $\frac{V_{mod}}{V_{fiss}}$  due to the small proportion of fissile material.

Due to safety reasons, PWR fuel assemblies are designed to be under-moderated, that is, below the optimum moderation ratio. As mentioned in the introduction, this has an effect on the reactivity of incomplete assemblies.

The number of MFR, denoted as  $n$ , is proportional to the moderation ratio (the ratio between the volume of water and the fissile material). Being the complete PWR assembly under-

moderated, reactivity increases with the number of MFR until it reaches a maximum value at the optimum moderation ratio, as illustrated in Figure 6.

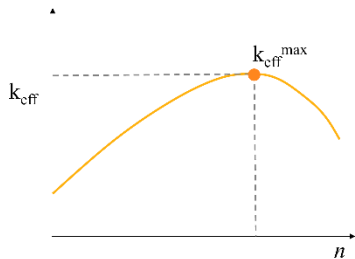


Figure 6. Scheme of  $k_{\text{eff}}$  as a function of the number of MFR.

Of course, the temperature (and hence density) of water modifies this reactivity curve, so an exhaustive study should take these parameters into account to consider all possible scenarios (e.g., the increase in temperature under accident conditions). However, the present work focused on other factors, and density was assumed to be that of room conditions.

To evaluate the criticality of the incomplete assembly, the traditional approach simplifies the assembly so that its moderation ratio (or  $n$ ) is preserved, but the spatial distribution of MFR is lost in the process (method explained in section 2.4.1

However, recent studies ([Dechenaux et al. 2023](#)) have shown that the placement of MFR significantly influences reactivity and cannot be neglected. For the same number of withdrawn fuel rods  $n$ , very different values of  $k_{\text{eff}}$  are found depending on the configuration, as illustrated in Figure 7, where differences in  $k_{\text{eff}}$  ( $\Delta k_{\text{eff}}$ ) up to 1000 pcm can be found. This large dispersion of results is referred as the “variability of the iso-moderation” ([Dechenaux et al. 2023](#)).

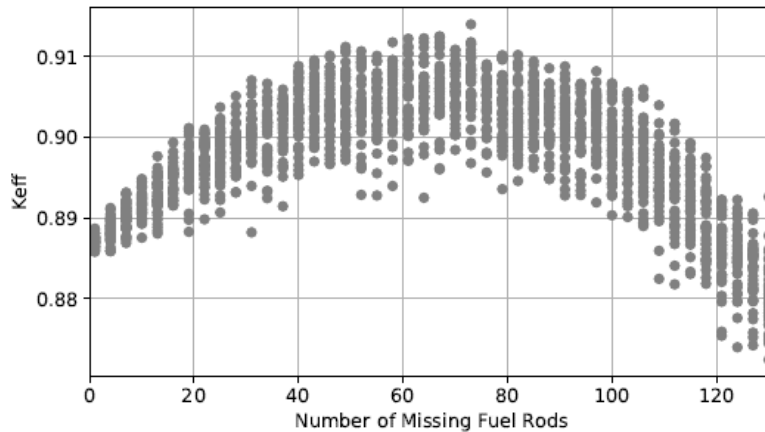


Figure 7.  $k_{\text{eff}}$  as a function of the number of MFRs for an isolated assembly. For a given number of MFRs, around 40 geometrical configurations are calculated. Source: [Dechenaux et al. 2023](#).

A rigorous criticality-safety assessment should demonstrate the subcriticality of all potentially encountered cases to find the most penalizing ones. However, the number of possible cases is extremely high. For a given number of MFR  $n$  in a square assembly of size  $N \times N$  (where  $n$  is the number of pins in one side of the square) the number of possible patterns is the combinatorial:

$$\binom{N^2}{n} \quad (5)$$

For all the possible  $n$ , assuming it can go from 0 to the total number of pins of the assembly  $N^2$ , the number of patterns is:

$$\sum_{n=0}^{N^2} \binom{N^2}{n} = 2^{N^2} \quad (6)$$

Some of the configurations are equivalent by symmetry and rotation. Indeed, from a neutronic point of view, configurations A and B in Figure 8 are virtually equal.

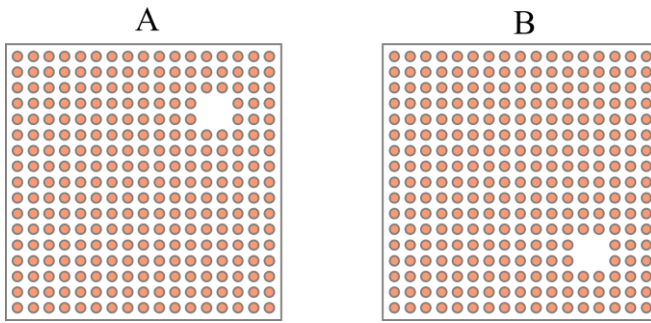


Figure 8. Example of two equivalent configurations (A transformed in B by rotation of  $90^\circ$ ).

However, even when removing these cases and leaving only the “unique” patterns, the amount remains too high to be feasible, as can be seen in Table 1, which illustrates the number of unique configurations for different values of  $n$  (the number of MFR) in the  $17 \times 17$  assembly.

Table 1. Number of unique possible configurations for a given number of MFR in the  $17 \times 17$  assembly ( $N=289$ ). Equivalent configurations by symmetry and rotation have been removed.

Number of MFR $n$	3	5	10	50	100	200
Number of unique configurations	$5.0 \cdot 10^5$	$2.0 \cdot 10^9$	$1.2 \cdot 10^{17}$	$5.0 \cdot 10^{54}$	$5.5 \cdot 10^{78}$	$2.0 \cdot 10^{75}$

### 2.3 Calculation Codes

To analyse nuclear systems, two approaches exist:

- **Deterministic approaches:** These study the neutron flux using the Boltzmann neutron transport equations or simplified versions of the equations (such as diffusion equation). The accuracy of the results depends on the assumptions made during the modelling process,
- **Stochastic approach: Monte Carlo.** In this method, the focus shifts from the entire neutron population (flux) to the behaviour of individual neutrons. The neutron's random walk from one interaction to the next is tracked. The probability and outcome

of each interaction are determined from probability distributions that represent the laws of physics. By tracking a large number of neutrons, the average behaviour of the system is estimated. The accuracy of this approach depends on the statistics: it improves with a larger sample size.

While deterministic codes obtain a detailed particle flux distribution and are generally faster, they can lead to inaccuracies in highly heterogeneous materials or complex geometries. The Monte Carlo approach allows more accurate geometry description and has the potential to produce highly accurate results. However, they are limited by relatively long computational times and the inherent stochastic nature of their results.

Monte Carlo reactor physics codes are typically used in nuclear criticality safety because of the high level of accuracy required and the frequent presence of complex geometries. SERPENT2 ([Leppänen, 2015](#)) is a Monte-Carlo code developed by VTT Technical Research Centre of Finland. Apart from criticality calculations, some other features of SERPENT are:

- Capability to introduce user-defined detectors and to get the four factors from the four-factor formula,
- Fission matrix capability. Despite being an undocumented feature, SERPENT can tally fission matrices in a set of fixed-source or a criticality calculation ([Rau, 2019](#)).

Complementing SERPENT's functionality, SERPENTTools is a very useful Python package for the post-treatment of the output files from SERPENT, which are written in Matlab m-file format. The package contains a variety of parsing utilities, each designed to read specific output from the SERPENT Monte Carlo code ([SERPENTTools, 2017-2019](#)).

## 2.4 Review of Literature: Approaches to Treat Incomplete Assemblies in Criticality Safety – Description of the Contact Surface Method

The traditional approach to model the problem does not consider the spatial distribution of the MFR, but only their number, in what we can call the “homogeneous” method. Different methods have been proposed in the last years to model the effect of the spatial distribution, driven by the impossibility to explicitly study all the possible configurations. Previously

mentioned, these methods are now discussed in more detail, along with the traditional, homogeneous method.

#### 2.4.1 Homogenization Method

Developed in the 80s, the homogeneous method creates an elementary cell representing the incomplete assembly: a fuel rod surrounded by water where the moderation ratio is equal to the one of the incomplete assembly. For the infinite lattice of the elementary cell, transport equation is deterministically solved and the multigroup cross sections are obtained. The material defined by these cross sections fills the total assembly. Monte Carlo calculations over this homogenous assembly give the  $k_{\text{eff}}$  for the incomplete assembly, where the spatial distribution of the MFR has been erased. Figure 9 illustrates this method.

At Framatome these steps are done within the CRISTAL V2's multi-group route APOLLO2-MORET5. Everything related to this route is described in [IRSN, 2024](#).

The CRISTAL package is a criticality safety calculation tool developed to enhance safety and mitigate criticality risks. Widely utilized by French criticality safety practitioners, including IRSN, CEA and industry, it supports both projects in France and abroad. First released in 2014, the package became available to the international community in 2018 through the NEA Data Bank.

The CRISTAL package offers three calculation routes to address all calculations needs for criticality safety assessments, ranging from standard calculations to detailed 3D modeling of systems: Multi-group deterministic route using APOLLO2 calculations, multi-group Monte Carlo route utilizing APOLLO2 and MORET 5 codes, and point-wise Monte Carlo route employing the TRIPOLI-4 code. All calculation routes rely on the CEAV5.1.2 cross-section library, generated by the same processing tool based on the JEFF-3.1.1 evaluation.

As mentioned, the route used by Framatome to treat incomplete assemblies is the APOLLO2-MORET 5.

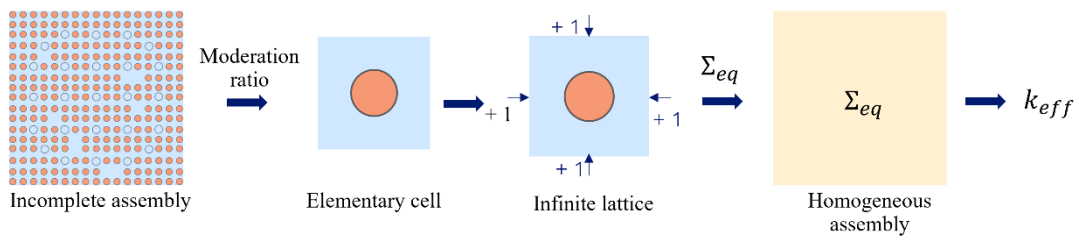


Figure 9. Scheme of the CRISTAL procedure for the homogenisation method.

Until 2017, the homogeneous approach was not challenged. It was easy, fast, and considered to give the maximum possible values, so the elimination of the MFR positions was considered as a good simplification. Afterwards, results from the homogenization were compared to more specific Monte Carlo calculations, and some of the configurations of the latter showed to be more reactive than the traditional results. That is; the specific pattern of the MFR has an impact on reactivity that can lead to greater values of  $k_{eff}$  than the ones obtained by the traditional method of homogenization.

For instance, for the isolated assembly with 25 MFR and the pattern shown in Figure 10, the homogenisation method underestimates  $k_{eff}$  by 800 pcm ([Albert et al., 2019](#)).

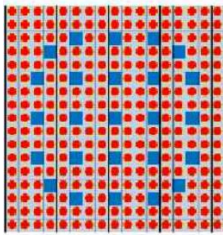


Figure 10. A pattern of 25 MFR in a 17×17 assembly.

In an attempt to solve this underestimation, a modification was added to the method: from the 1-zone method, a 2-zones method was developed. Information about this modification can be found in [Hoefler, 2019](#) and [Albert et al., 2019](#). Figure 11 shows the two zones within the assembly.

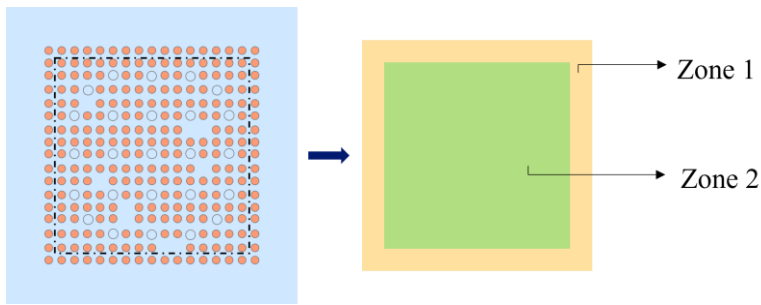


Figure 11. Two-zone model of the homogenised fuel assembly.

- Zone 1 contains the fuel rods in the periphery of the assembly, where it is assumed that there are no MFR, to minimize neutron leakage,
- Zone 2 corresponds to the fuel rod positions in the interior of the fuel assembly where the moderation is continuously varied and tuned to be a value of optimum moderation.

While the 1-zone method underestimates the reactivity for some configurations, the 2-zones method is too penalizing for some cases. The reactivity of pattern in Figure 12 is overestimated by the 2-zones method by 1100 pcm ([Albert et al., 2019](#)).

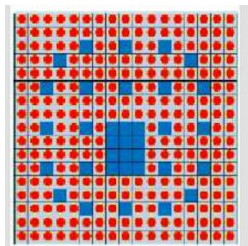


Figure 12. A pattern of 35 MFR in a  $17 \times 17$  assembly.

The overestimation of reactivity, along with its lack of physical justification, caused this method to be unsatisfactory for the operator.

### 2.4.2 Assumption of Ad Hoc Hypothesis

The alternative proposed methods to the homogenization aim at an intelligent reduction of the sample of configurations, that would anyway give the most reactive cases. A simple, first attempt makes ad hoc hypothesis about certain characteristics of the supposed optimal configurations, like the general idea that the most reactive ones do not have MFR in their periphery ([Duquenne et al., 2023](#)). However, due to the lack of physical support and verification of these hypothesis, the success to find the most penalizing cases is not guaranteed by such a type of analyses.

### 2.4.3 Optimization Algorithms

In the category of optimization algorithms, Generational Genetic Algorithms (gGA) employed by CEA stand out. The information related to this method comes from [Dupas, 2023](#). The gGA's objective is to maximize the neutron effective multiplication factor,  $k_{\text{eff}}$ , by cleverly generating different configurations (aka patterns) with a given number  $n$  of missing rods. Again, results prove that in some cases heterogeneous calculations with individual missing rods modelled are more penalizing than the homogeneous approach.

The gGA's application to the MFR problem treats configurations as chromosomes. Figure 13 represents the encoding of one configuration to a chromosome.

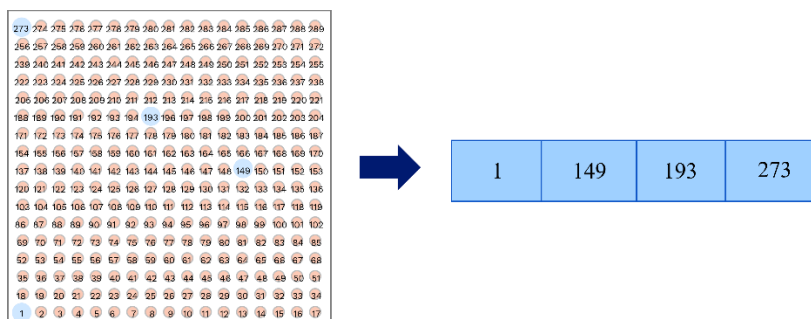


Figure 13. Incomplete assembly (left) and its corresponding chromosome (right).

The general mechanism is the following: from an initial population of chromosomes, the population is replaced by its offspring throughout the iterations. At each iteration, the current population (the parents) give place to a new population (the offspring) by means of special techniques of the gGA. The  $k_{\text{eff}}$  linked to a pattern is referred as the fitness, and the goal of the gGA is to enhance the population's fitness over successive generations.

Figure 14 depicts the most penalising pattern found by CEA with their gGA for their 16×16 assembly.

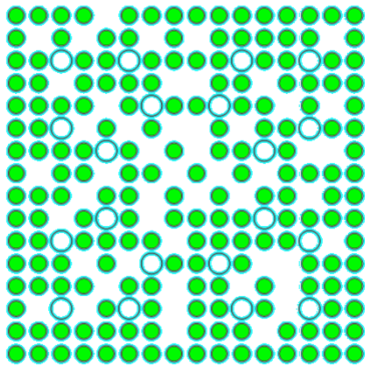


Figure 14. Most penalising pattern in a 16×16 assembly found by CEA with gGA.

A total of 50 fuel rods have been withdrawn (plus 20 guide tubes, that are considered as MFR) and its effective multiplication factor is  $k_{\text{eff}} = 0.981$  ([Dupas, 2023](#)).

#### 2.4.4 Contact Surface Method

The main idea behind this method is the intuition that one parameter must exist to complement the number of MFR  $n$ , explaining the iso-moderation variability of  $k_{\text{eff}}$  that Figure 7 previously illustrated. In line with the aim to reduce the sample of configurations, such a parameter would be able to find a “physical equivalence” between configurations and classify them according to it. The parameter proposed by IRSN for this purpose is the so-called “contact surface”. Everything related to this parameter and its calculation is described in [Dechenaux et al. 2023](#).

This purely geometric parameter is constructed as illustrated in Figure 15. The incomplete assembly is conceived as cartesian lattice. Two types of cells are found in the mesh: the empty cells at the location of the MFR and the fuel cells, containing a fuel pin in its centre. The assembly is converted in a binary mixture of empty and fuel partitions.

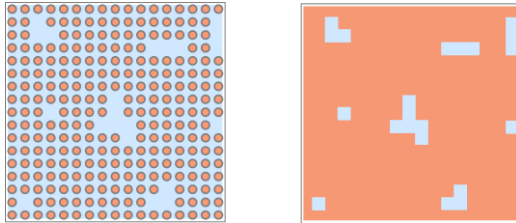


Figure 15. Incomplete assembly (left) and its interpretation as random binary mixture (right).

The contact surface  $S$  is defined as the perimeter of the interface between these two media, where each side of a cell has by convention a unitary length. In other words, it is the number of edges of such border between media. Figure 16 exemplifies this calculation for a region of the incomplete assembly.

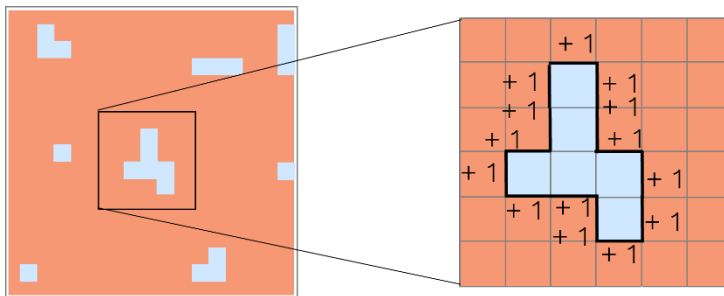


Figure 16. Example of the calculation of  $S$ : +1 for each edge in the frontier between the two materials.  $S = 14$  in the example.

A criterion must be chosen for the interface between the fuel pins in the periphery of the isolated assembly and the surrounding water. The criterion chosen is to count the edges at the boundary assembly-environment and include them in the calculation of  $S$ . The convention implies that even the complete assembly has  $S > 0$ . For instance, a complete  $17 \times 17$  assembly has  $S = 17 \times 4 = 68$ . We define this offset quantity as  $S_{\text{border}}$ .

Rather than working with the absolute value of  $S$ , which is obviously very correlated to  $n$ , a normalized surface contacts is used, defined as

$$s = \frac{S - S_{border}}{4 \times n} \quad (7)$$

where  $4 \times n$  represents the maximum value of the interface, since each MFR can have 4 neighbours at maximum. To be able to have  $s=0$ , the offset of  $S_{border}$  is also included in the normalization. By these means, the normalized surface  $s$  is usually bounded between  $[0, 1]$ . In fact, some configurations may end up with negative values of  $s$ . Figure 17 exemplifies this possibility.

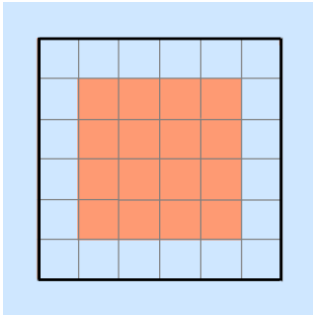


Figure 17. Binary mixture representing an assembly where  $s < 0$ . For the example:  $S=16$ ,  $S_{border}=24$ ,  $n=20$ ,  $s = -0.1$

This situation can be ignored as the configurations having negative  $s$  are certainly not the most reactive ones. On the other hand, in a  $17 \times 17$  assembly for  $n > 112$ ,  $s = 1$  is not attainable since it is geometrically impossible to have all MFR with 4 fuel pins as neighbours.

In this work, the normalised contact surface  $s$  will be referred as the contact surface. The hypothesis was that the contact surface method should be able to:

- Group configurations having the same number of MFR  $n$  and the same contact surface  $s$  so that they present similar values of  $k_{eff}$ ,
- Among these configurations, the most reactive are grouped as the ones having the greater values of  $s$ .

## 2.5 Metropolis-Hastings Algorithm: A Useful Tool for the Contact Surface Method

When generating different sets of configurations, it can be useful to apply specific algorithms capable of favouring configurations with a targeted contact surface value  $s$ . This eases the validation of the recently proposed hypothesis of the contact surface method. The Metropolis-Hastings algorithm (MH) can be used for that purpose. It is a Markov chain Monte Carlo (MCMC) method for obtaining samples from distributions that may otherwise be difficult to sample. The sequence of generated samples converges to the desired distribution  $\pi$ . MH algorithms are particularly useful for sampling from multi-dimensional distributions, as it is the case of our problem.

A key element of the MH is the “transition kernel”, used to propose new samples. The transition kernel  $Q(x|y)$  is the probability distribution of a new position in space  $y$  given a current position  $x$ . A common choice is the so-called “random walk”, which centres the proposal distribution over the current position, so that the points in its vicinity are more likely to be visited next.

The pseudo code for the MH algorithm that samples from a target distribution  $\pi$ , by means of a transition kernel  $Q$ , is presented below. The  $t$  index represents the number of the iteration,  $y$  is the candidate value for  $x_{t+1}$  from  $x_t$ . The initial value  $x_{\text{init}}$  can be either user-defined or extracted from a given distribution ([Taboga, 2021](#)).

Algorithm 1. Generic Metropolis-Hastings algorithm.

---

1. Initialize  $x_1 = x_{\text{init}}$

2. For  $t = 1, 2, \dots$

Generate  $y$  from  $Q(x_t|y)$

Compute

$$A = \min\left(1, \frac{\pi(y)Q(x_t|y)}{\pi(x_t)Q(y|x_t)}\right) \quad (8)$$

3. Take

$$x_{t+1} = \begin{cases} y & \text{with probability } A \\ x_t & \text{with probability } 1-A \end{cases}$$


---

$A$  is often called the “acceptance probability”. It represents whether it is more plausible for the new point to be a sample of the target probability distribution, the latter being controlled by the ratio of probabilities for the old and new points ([Dechenaux, 2023](#)).

A kernel that satisfies  $Q(y|x) = Q(x|y)$  for all  $x, y$  is called “symmetric”. This is the case, for instance, of the random walk kernel. A symmetric kernel simplifies the acceptance probability to:

$$A = \min\left(1, \frac{\pi(y)}{\pi(x_t)}\right) \quad (9)$$

This case of the Metropolis-Hastings algorithm is sometimes named as the “Metropolis algorithm”.

The application of MH algorithm to the specific case of incomplete assemblies is described in 3.1.2

### 3 Methodology: Modelling Incomplete Assemblies and Application of the Contact Surface

The first step of the research was the verification of the impact of MFR spatial distribution on reactivity. For a  $17 \times 17$  assembly, samples of patterns of MFR were created for a wide range of number of MFR  $n$ . The reactivity of these samples was evaluated and a similar curve to the one previously presented in Figure 7 was obtained as a preliminary result. These initial results showed the importance of a systematic approach in MFR modelling, like the contact surface method.

The work implemented and studied the contact surface method and its hypothesis, along with the comparison of its results to the results from gGA. To test the relation between the contact surface  $s$  and  $k_{\text{eff}}$ , samples of configurations were created, and criticality calculations of these configurations were done. Three major activities with their associated tools were carried out: Creation of the inputs for the criticality calculations, criticality calculations and post treatment of outputs from the criticality calculations. The methods and tools for these activities are now explained in more detail.

#### 3.1 Methods For the Generation of Configurations: How to Create the Patterns

The approaches to create the samples of configurations are now presented.

##### 3.1.1 Random Generation

In the cases where the total number of combinations is reasonably low, all possible configurations were created and run, in what we can call an exhaustive generation of configurations. Python scripts were programmed to obtain these configurations and verify that the amount generated correspond to the number of unique possible configurations.

However, as explained in the introduction, the number of potential combinations is usually too large to be feasibly studied. To address this, a subset of configurations was generated and run. Once again, Python scripts were developed to generate random MFR patterns within

an assembly. These scripts also calculated the contact surface for each pattern. Yet, it turned out that this purely random selection was not a representative sample of the configuration space, or at least, not an intelligent one. Figure 18 represents the results of a random generation for  $n=80$ .

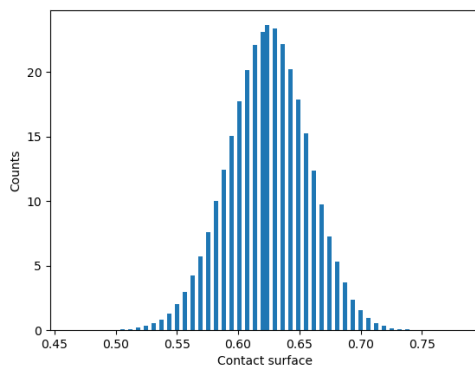


Figure 18. Histogram of the distribution of the contact surface for a sample of 106 randomly generated configurations, with  $n = 80$  in the  $17 \times 17$  assembly.

Despite having created 106 configurations, the distribution of  $s$  was concentrated around the mean value of 0.6, and it was extremely rare to find configurations with  $s > 0.75$  or  $s < 0.5$ . This behaviour was not specific to the case  $n=80$ .

Figure 19 reproduces the distribution of  $s$  to every possible  $n$ , so that the distribution of configurations in the whole  $(n, s)$  space is shown.

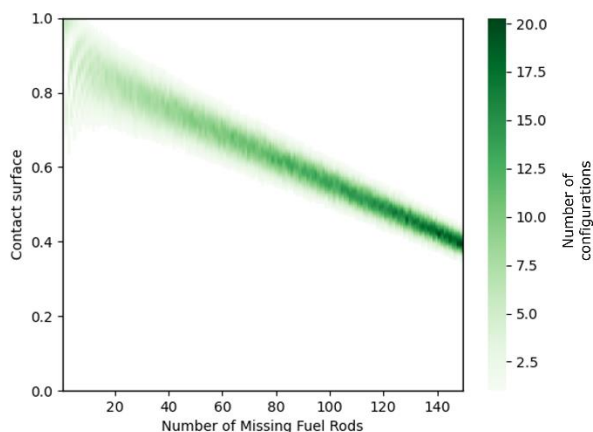


Figure 19. Distribution of the configurations in the  $(n, s)$  space. For each number of MFR, 1000 random configurations were generated.

Again, the configurations are concentrated in a very specific region, leaving the most part of the  $(n, s)$  space with very few configurations. Up to  $10^{80}$  iterations would be needed to randomly get a configuration that falls in this “rare” regions, so another method rather than the random generation must be put in place to access these regions and be able to study a wide range of  $s$ . Moreover, the configurations with very high values of  $s$  ( $s \approx 1.0$ ) fall within these regions, while the contact surface method establishes the hypothesis that higher  $s$  may lead to higher reactivities. Therefore, a random generation would bypass the rare, most reactive configurations. Again, this proves the necessity of an alternative mechanism to reach these rare, hypothetically more reactive cases.

Besides this,

Figure 19 illustrates the general trend of  $s$  with increasing  $n$ : the mean value of the contact surface decreases as the number of MFR grows, since it progressively becomes less probable to find isolated MFR.

### 3.1.2 Biased Generation

Responding to this need, the random generation was substituted by a biased generation capable of favouring the configurations with high surface. The Metropolis-Hastings algorithm described in 2.5 fills such need.

To implement the MH algorithm to our specific problem, the target distribution  $\pi$  must favour the configurations with the desired  $s_{\text{target}}$ , for a given number of MFR  $n_0$ . To do so, the natural choice was to generate configurations along a Gaussian probability distribution like:

$$\pi(x) \propto e^{-\frac{(s(x)-s_{\text{target}})^2}{2\sigma^2}} \quad (11)$$

where  $s(x)$  is the contact surface of the configuration  $x$ , and  $\sigma$  is set as the acceptable standard deviation of the distribution.

Metropolis-Hastings got to sample elements from this probability distribution by starting from a randomly chosen configuration (thus located in the probable region of the configuration space) and applying to it successive modifications, by means of the transition kernel  $Q$ . This way, the MH algorithm was able to generate a great sample of configurations with the desired contact surface through few iterations (between  $10^4$  and  $10^6$  iterations) compared to number of random draws needed to get rare configurations (about  $10^{80}$  draws).

Developed in Python, the ultimate outcome of the method was a set of *unique* configurations with the aimed  $(n, s)$  pairs, ready to be run by SERPENT. Applied to the range of possible values of  $n$  and  $s$ , this method was used to pave the whole  $(n, s)$  space.

### 3.2 Criticality Calculations: How to Evaluate $k_{\text{eff}}$ of the Generated Configurations

SERPENT2 Monte Carlo reactor physics code was used in this work to compute parameters describing criticality of fuel assemblies. SERPENT2 and its features were introduced earlier in section 2.3 Calculated parameters included  $k_{\text{eff}}$ , six-factor formula or fission matrix.

Regarding the parameters of the simulations, the number of inactive cycles was set to 50, followed by 1000 active cycles, each of them of 40000 neutrons, resulting in a total of  $4 \times 10^7$  neutrons and a standard deviation of  $\sigma < 30$  pcm. The order of magnitude of  $\sigma$  used by Framatome in criticality assessments is usually 100 pcm. However, being the objective to test how good was  $s$  at grouping configurations by their  $k_{\text{eff}}$ , very precise results were needed. Such a low standard deviation allowed to clearly distinguish configurations assuring that their difference in reactivity stood on their different spatial distributions and not on the associated uncertainty.

JEFF-3.1.1 library provided the nuclear data required for the calculations. In any case, there was no particular interest in the choice of the library since it was not the aim of the work to compare results between codes or libraries.

### 3.3 Python Programming: Task Automation

Python scripts were specifically developed to automate several tasks related to the input and output files for SERPENT, some of which mentioned in previous subsections. Throughout

the research (the steps of which are illustrated in Figure 20), the following tasks were performed by Python scripts:

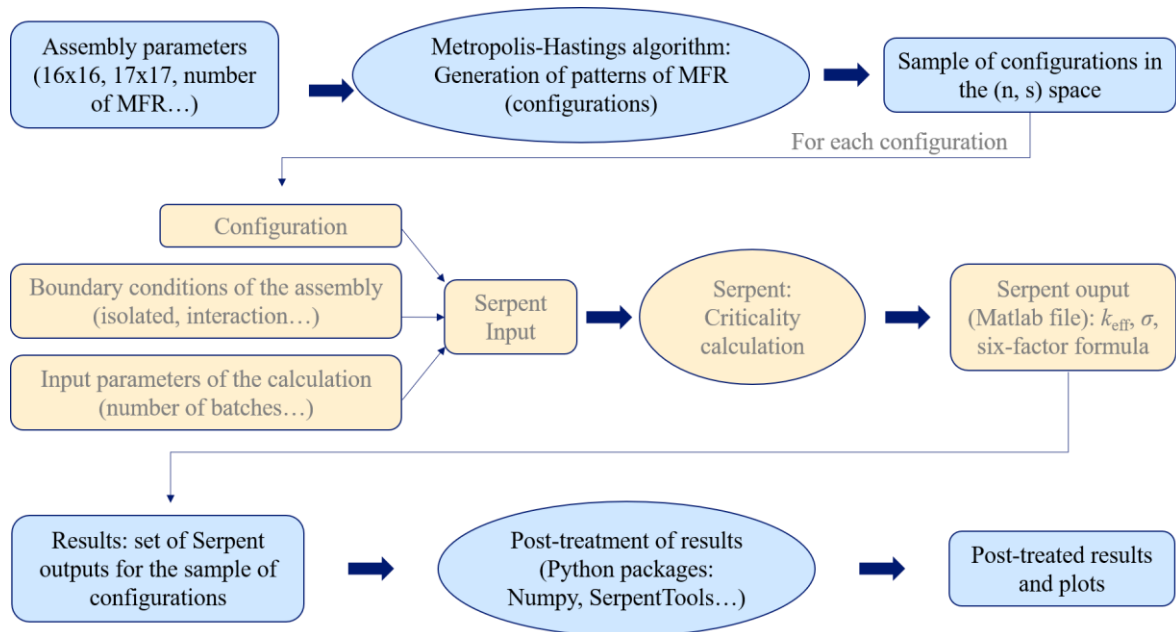


Figure 20. Schematic representation of the methodology.

- Generation of the configurations of incomplete assemblies with the methods presented in 3.1
- From configurations, creation of the input files for SERPENT,
- Modification of inputs to establish new boundary conditions or modify parameters,
- Post treatment of the results from SERPENT.
- Calculation of the contact surface  $s$  and other geometrical parameters of the patterns,

Some particularly useful libraries were Itertools, Numpy (for the manipulation of assemblies, treated as arrays), SERPENTTools for the post-treatment of the output files from SERPENT; Pandas, Matplotlib and Seaborn for the representation of the results.

### 3.4 Study Cases: Parameters of the Generated Configurations

The study case was the axially infinite PWR UO<sub>2</sub> assembly immersed in water, with variable number and position of MFR. The specific characteristics of this assembly were modified at each stage, giving place to several study cases, synthesized in Table 2 .

Table 2. Synthesis of the different study cases.

	Composition (A)					Composition (B)
Study cases	Case 1	Case 2	Case 3	Case 4	Case 5	Case 6
Enrichment	A	A	A	A	A	B
Pitch (cm)	A	A	A	A	A	B
Guide tubes	No	No	No	No	No	20
Environment	Isolated (Water)	Isolated (Water)	Water-concrete	Water-concrete	Array	Isolated (Water)
Size <i>N</i>	5	17	5	17	17	16

Two types of fuel pins (different in terms of enrichment and pitch) were used, here referred as A and B. The following subsections provide a more detailed overview of the different study cases and their objectives. Additional figures related to the study cases can be found in Appendix 1.

#### 3.4.1 Study Cases for the Application and Validation of the Method

These study cases were the ones isolated by 20 cm of surrounding light water. No guide tubes or maximum number of MFR were imposed, to keep the case as more general as possible.

- Study case 1. The research started by the “Fictional” 5×5 assembly due to the ease to manipulate it. The number of possible configurations was still enormous (4 211 744) but the application of a constraint considerably reduced the sample so that it

became feasible to be exhaustively evaluated. The following constraints were applied alternatively:

- Setting the number of MFR at  $n = 4$  MFR. The 1666 configurations for this case were studied.

In Figure 21 the results of  $k_{\text{eff}}$  as a function of  $s$  indicate the capacity of the contact surface parameter to group configurations by their reactivity.

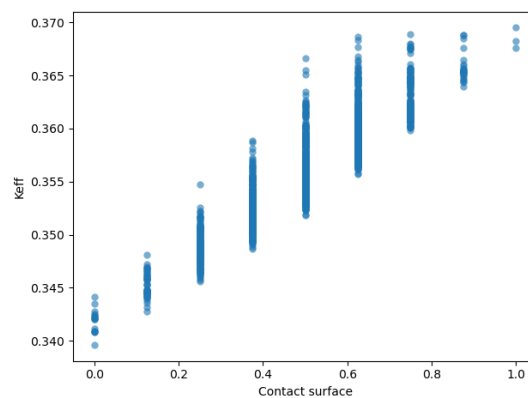


Figure 21.  $k_{\text{eff}}$  as a function of  $s$  for 4 MFR in the  $5 \times 5$  isolated assembly.

However, for some cases (intermediate values of  $s$ ) the variability of  $k_{\text{eff}}$  is also very high ( $>1000$  pcm) despite having the same contact surface. In other words: Figure 21 shows how the variability in the iso-moderation is not completely explained by  $s$ .

This “residual variation” appeared in further cases and was subjected of improvement since it represented a limitation of the contact surface method.

- No MFR in the periphery. Studies ([Albert et al., 2019](#)) are proving that the most reactive configurations present all their fuel rods in the periphery. By imposing that no MFR could be found in the periphery of the assembly, the number of configurations dropped to the number for the  $3 \times 3$  assembly, that is; 101 cases. Figure 22 shows the distribution of the contact surface of configurations for each possible number of MFR, from 1 to 9. The poor variety of the contact surfaces values can be noticed. In fact, it was not

possible to get high values of  $s$  for  $n > 5$ . This already gave a hint of the limitations of the  $5 \times 5$  assembly for the study.

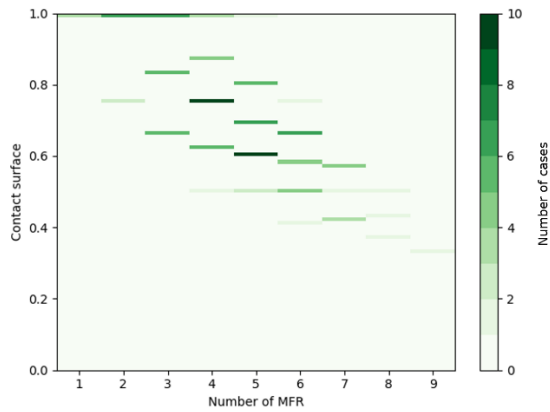


Figure 22. 2D histogram of the distribution of the configurations for the isolated  $5 \times 5$  assembly, no MFR in periphery.

A few more configurations were added, this time allowing the presence of MFR for the periphery. For  $n > 5$ , the cases with higher contact surface were built and run in SERPENT. These 5 additional cases, along with their respective  $s$  are presented in Figure 23.

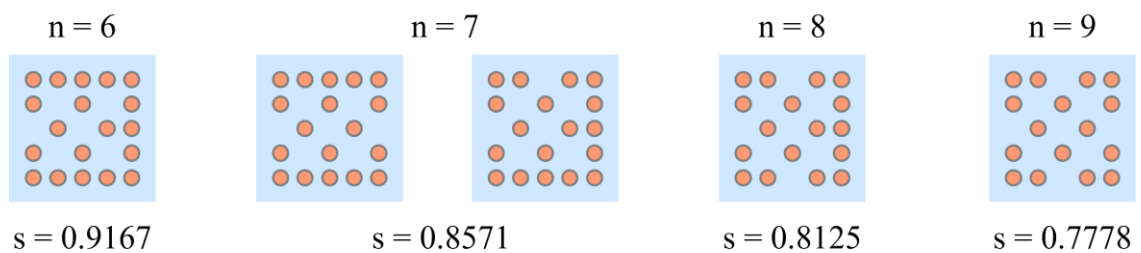


Figure 23.  $5 \times 5$  configurations with MFR in periphery, along with their values of  $s$ .

The poor variability of  $s$ , even when MFR were allowed in periphery, and the impossibility to test the effect of a very high  $s$  with more than 5 MFR, indicated the limitations of this first study case to explore the method. For this reason, the  $17 \times 17$  case was studied, as explained in next section.

- Study case 2: Realistic  $17 \times 17$  assembly.

In the case of the  $17 \times 17$  assembly, an exhaustive generation of configurations was unfeasible. Samples of configurations were first created randomly, and later generated using the MH algorithm:

- Random generation. As a first step, a completely random generation was performed. Figure 24 presents the results of this random generation, done as explained in section 3.1.1. 50 random cases were created of each number of MFR, making a total of 1470 cases<sup>2</sup>.

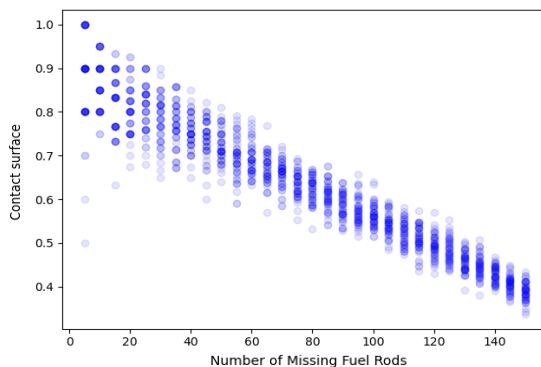


Figure 24. Distribution in the  $(n, s)$  space of the 1470 configurations randomly generated.

As

Figure 19 already illustrated in section 3.1.1 the sample presented very specific values of contact surface. The results of  $k_{\text{eff}}$  were expected to be less significant due to this lack of diversity in the contact surface values; nevertheless, the sample was run, and  $k_{\text{eff}}$  results were also obtained.

- MH generation. The first generations by MH algorithm aimed at a target surface between 0.6 and 1: 779 cases were created. Secondly, MH was used to aim at very high contact surface, generating 1226 configurations with  $0.9 < s < 1$ , in an attempt to find the upper-bounded curve.

Finally, MH was used for a thorough analysis of the residual variation phenomena.

To do so, configurations with  $s = 0.6$ ,  $s = 0.8$ ,  $s = 1$  (with  $\sigma = \pm 0.01$ ) were created for

---

<sup>2</sup>There are less than 50 different configurations for some values of  $n$ . In such cases, the maximum possible number of configurations was done.

different values of  $n$  (20, 40, 60, 80, 100). 1050 configurations were generated in total, with 70 for each  $(n, s)$  pair.

### 3.4.2 Study Cases for the Application of New Boundary Conditions

In the second phase of the research, the contact surface method was challenged by changing the isolated assembly for two different boundary conditions: Water-concrete boundary conditions and the array of assemblies. In particular, the study cases were modified to:

- Study cases 3 and 4: Water-concrete cases (Figure 25). One meter of concrete surrounded the assembly from the upper and left side, while water occupied the low and right sides. These boundary conditions replicated the potential situation where the assembly was located in a corner of the (spent) fuel storage pool. The hypothesis was that the contact surface method would give less precise results for the water-concrete case with respects to the isolated case (that is, a wider residual variation), being the MFR in the periphery in contact with different materials.

Since the symmetry was “broken”, more unique cases appeared for this study case. Some configurations were no longer equivalent due to the concrete walls (example in Figure 64 in Appendix 1).

The water-concrete environment was applied both to the  $5 \times 5$  and the  $17 \times 17$  assembly, giving place to study cases 3 and 4:

- Study case 3:  $5 \times 5$  assembly, with the constraint of no MFR in periphery, resulting in 287 different configurations.
- Study case 4:  $17 \times 17$  assembly. To verify the hypothesis, the water-concrete conditions were applied to the same sample of configurations with  $s=0.6$ ,  $s=0.8$ ,  $s=1$  generated by MH for the isolated case. The rotations of these configurations, no longer equivalent, were also run, widening the sample to 3150 configurations (70 for each  $(n, s)$  pair).

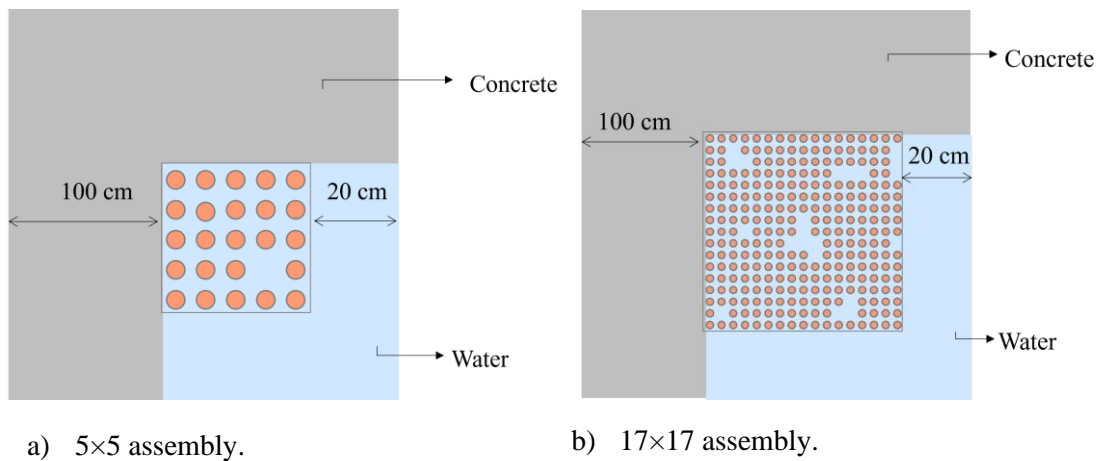


Figure 25. Schemes of the water-concrete boundary conditions. Non-proportional dimensions in the drawing.

- Study case 5: Array case. The interest of this composition was that it simulated the industrial situation of the storage of assemblies. Periodic boundary conditions were imposed to the isolated assembly and the surrounding water thickness was reduced to different values to test the effect of the distance between assemblies. The distances were defined as multiples of the nominal pitch: 1, 2, 5 and 10 times the pitch. The array environment was only applied to the 17×17 assembly.
  - For the first results, the number of MFR was fixed to 40. MH was used to generate 20 configurations for each value of  $s$  ( $s=0.6$ ,  $s=0.8$ ,  $s=1$ ) and each distance between assemblies (1, 2, 5 and 10 times the pitch), with a total of 240 configurations.
  - The case  $n=40$ , distance=5×pitch was then studied in more detail. For  $s=0.2$ ,  $s=0.4$ ,  $s=0.6$ ,  $s=0.8$ ,  $s=1$  and different values of  $n$  (20, 40, 60, 80, 100, 110), MH generated 1500 configurations in total, with 50 for each  $(n, s)$  pair.

### 3.4.3 Study Cases for the Comparison of the Results

The CEA research in incomplete assemblies focused on an isolated  $16 \times 16$  assembly with 20 guide tubes in fixed positions ([Dupas, 2023](#)), as can be seen in Figure 26.

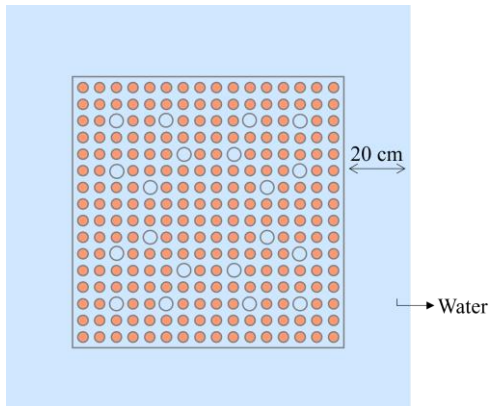


Figure 26. Study case 2: Isolated  $16 \times 16$  assembly with 20 fixed guide tubes.

The most penalising pattern found by CEA with the gGA for this assembly contains 50 absent fuel pins, plus the 20 guide tubes. With guide tubes treated as MFRs, the total number of MFRs ( $n$ ) is 70. The pattern appears in Figure 27.

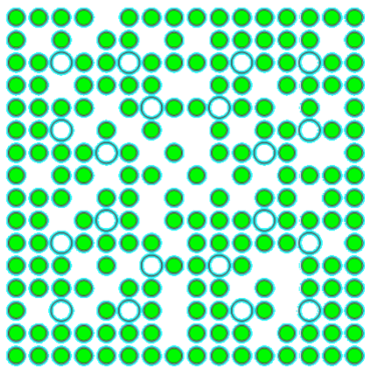


Figure 27. Most penalising pattern CEA, for study case 2. Source: [CEA, 2023](#).

The first step of the research in this part was to repeat the criticality calculation of the assembly in Figure 27 to verify that the result from our SERPENT calculation was consistent

with the reference from CEA:  $k_{\text{eff}}=0.981$  (Dupas, 2023). The result was  $0.9814 \pm 20$  pcm; from now on referred as  $k_{\text{eff}}^{\text{CEA}}$ . The contact surface of the pattern was  $s_{\text{CEA}}=0.8357$  (the 20 guide tubes were accounted in the calculation of  $s$  too).  $k_{\text{eff}}^{\text{CEA}}$  and  $s_{\text{CEA}}$  were used in the research as reference values to compare with the results generated by MH algorithm.

The MH algorithm was used to generate configurations with the same number of MFR that the pattern from CEA; that is  $n = 70$ . The algorithm was modified to impose the positions of the 20 guide tubes<sup>3</sup> and place the other 50 MFRs in the remaining positions.

MH was alternatively used for the following generations:

- Firstly, configurations with  $0.8 < s < 1.0$  were created and run, with the aim to find the most reactive configurations. 10 configurations were generated for each  $s_{\text{target}}$  in [0.8, 0.85, 0.9, 0.95, 0.99, 1].
- Secondly, in order to test the capability of MH to find reactive configurations in the region of  $s_{\text{CEA}}$  (0.8357), a greater sample with  $s$  around  $s_{\text{CEA}}$  was generated: 600 configurations with values of  $s$  ranging from 0.82 to 0.85. Among these 600 configurations, 200 had  $s$  exactly equal to  $s_{\text{CEA}}$ .
- Finally, the constraint of no MFR in the periphery was imposed. The gGA pattern does not present MFR in the periphery; while MH for  $s < 1$  tended to find patterns with MFR in the periphery. With the constraint of no MFR in the periphery, 500 new configurations were created with  $s$  exactly equal to  $s_{\text{CEA}}$ .

### 3.5 Some Useful Tools to Refine the Contact Surface Parameter

As it will be shown in the results, some “residual variation” was found in the results of the method. To deal with this limitation, two tasks were done:

- Observation of the neutronics behaviour of the configurations and correlation with  $s$  and  $k_{\text{eff}}$ ,

---

<sup>3</sup> These positions are fixed by the CEA. The guide tubes are treated as MFR for the calculation of  $n$  and  $s$  but are explicitly modeled in the SERPENT script with their cladding geometry and composition.

- Attempt to find another parameter to complement  $s$ , which could allow the prediction of the most reactive configurations.

The variables and new studies done to further study the incomplete assemblies are now presented.

### 3.5.1 Six-Factor Formula

The effect of each factor of the six-factor formula (Equation 4) in the  $(n, s)$  space was found. The goal was to identify the factors contributing to:

- a) The relation higher  $s$ –higher  $k_{\text{eff}}$ ,
- b) The dispersion of  $k_{\text{eff}}$  for a  $(n, s)$  pair.

SERPENT obtained the results for the whole study case, including the surrounding water, so the system did not present leakage. Therefore, instead of the six-factor formula, the four-factor (Equation 2) was used. The factors were analyzed for two samples:

- Same sample of configurations with  $s=0.6$ ,  $s=0.8$ ,  $s=1$  generated by MH for the isolated  $17 \times 17$  assembly, (Figure 36) when the residual variation was analyzed in detail (70 configurations for each  $(n, s)$  pair).
- Results of the four-factor formula were also obtained for the CEA pattern as well as for the configurations obtained with MH for the study case of CEA with  $s=s_{\text{CEA}}$ .

### 3.5.2 Detectors

Detectors were applied to the three configurations in Table 3 to have a deeper insight of their neutronic behaviour. Reaction rates (fission, elastic scattering, and absorption) in the assembly and in the fuel were obtained. Some ratios, such as the ratio of losses to total thermal flux and the ratio captures in water to captures in fuel were calculated. Reaction rates by energy of the neutron (thermal, epithermal, fast) were also studied.

To study the spatial distribution of the thermal flux and reaction rates, the assembly was divided into rings as illustrated in Figure 28. An external ring including the closest

surrounding water was also included. In SERPENT, spatial detectors were created in each of the rings to calculate different magnitudes of interest for each region.

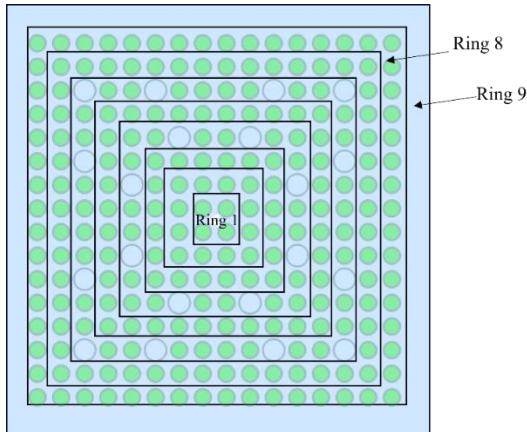


Figure 28. Partition of the assembly in rings for the spatial detectors.

### 3.5.1 Fission Matrix

The main objective was to explore the fission matrix and identify some pattern showing significant differences between configurations, and that could be linked to the contact surface.

To do so, the fission matrix of some configurations of study case 6 was evaluated. Three configurations with MFR in very specific regions were used. These regions were concentric rings of pins in the assembly, as shown in Figure 29. The aim was to see if the fission matrix provided information about the effect of having MFR in the inner or outer regions of the assembly.

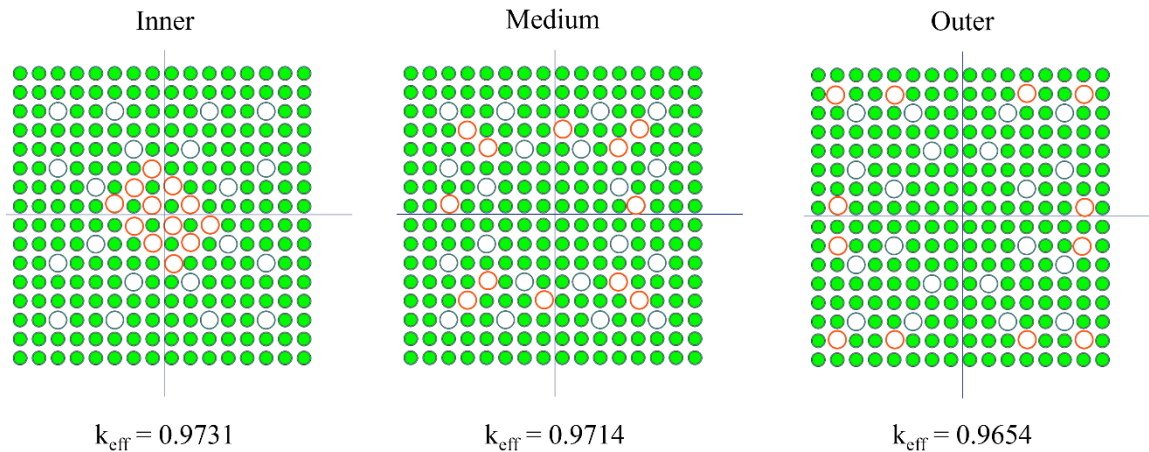


Figure 29. Three configurations of study case 6 used for the fission matrix. They all presented  $n = 12$  MFR and  $s = 1$ . The red circles represent the 12 MFR.

The partitions of the fission matrix were the concentric rings defined in Figure 30. Then, the fission matrix was a  $3 \times 3$  matrix where the element  $(i, j)$  contained the fissions induced in ring  $i$  by neutrons born in ring  $j$ .

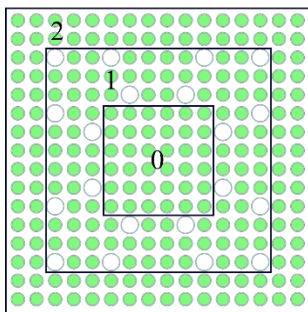


Figure 30. Regions of the assembly defining the partitions for the fission matrix.

### 3.5.1 Dispersion of the Contact Surface Within the Assembly

Next, the residual variation of the contact surface  $s$  was investigated. Since the contact surface  $s$  was defined earlier as a parameter describing the distribution of the MFR, the residual variation of  $k_{\text{eff}}$  can be due to the dispersion of this distribution. Variance is the measure of dispersion. In other words, to complement  $s$  (which can be seen as the mean,

normalised value of the number of fuel rod neighbours of the MFR in the assembly) a variance of  $s$  could be defined.

$N_{\text{neigh}}$  was defined as the distribution of the number of fuel rod neighbours of the MFR in the assembly. The number of fuel rod neighbours can vary from 0 to 4. The last value represents the case of a completely isolated MFR as seen earlier. This new parameter, called standard deviation of  $s$  ( $\sigma_s$ ) was defined to be the standard deviation of  $N_{\text{neigh}}$ .

The variable was first tested in the array case, as this particular case gave the results with the largest  $k_{\text{eff}}$  residual variation. After this test, it was then applied to the isolated  $17 \times 17$  assembly.

## 4 Results of Modelled Configurations and Their Relation to the Contact Surface

The initial results obtained were intended to confirm if the spatial distribution of MFR significantly impacts reactivity. From Figure 31 it can be seen that two incomplete assemblies were having quite different  $k_{\text{eff}}$  values ( $\Delta k_{\text{eff}} = 1000$  pcm) despite having the same number of MFR. The curve in Figure 32 illustrates this large variability of the iso-moderation: for the same number of withdrawn fuel rods, very different values of  $k_{\text{eff}}$  were found.

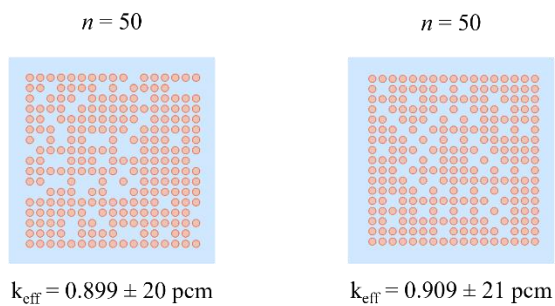


Figure 31. Two 17×17 incomplete assemblies with 50 MFR, immersed in water, and their respective multiplication factors. Surrounding water thickness truncated in the scheme.

One could be tempted to take the highest values of such curve as the maximum values for each number of MFR and consider the problem to be solved. However, such curve only represents a small sample of the huge number of different existing patterns and there is no prove that most reactive cases are all contained in this sample.

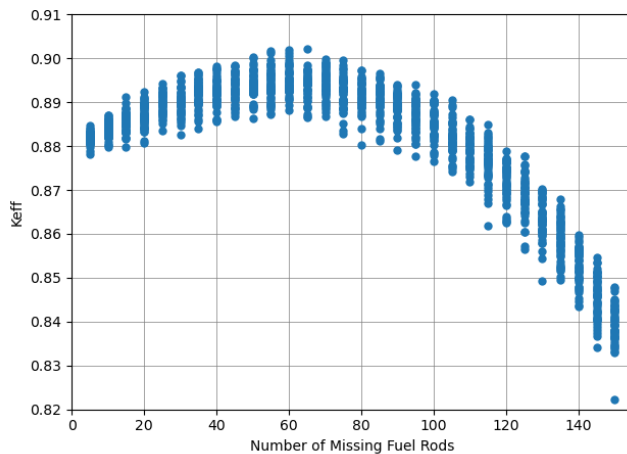


Figure 32. Results of  $k_{\text{eff}}$  for an isolated  $17 \times 17$  assembly as a function of  $n$ . For each  $n$ ,  $50^4$  configurations have been sampled.

Results are structured in a first part of implementation of the method (section 4.1 where the isolated assembly is studied), followed by the application to new boundary conditions in section 4.2 and the comparison with the gGA results in section 4.3 Attempts to refine the contact surface parameter close section 4.4 .

#### 4.1 The Isolated Assembly: Application and Validation of the Contact Surface Method

The results for the  $5 \times 5$  assembly and the  $17 \times 17$  assembly are now presented.

##### 4.1.1 Study Case 1: $5 \times 5$ Assembly

After the first results for  $n = 4$  (Figure 21) results for all possible configurations with no MFR in the periphery were found. Results of  $k_{\text{eff}}$  as a function of the number of MFR, with a third variable representing  $s$  are shown in Figure 33. The results of the 5 specific cases with MFR in periphery (Figure 23) are included too.

The results are aligned with the hypothesis of the method (section 2.4.4):

---

<sup>4</sup>To be exact: 50 or the maximum number of possible configurations for a given  $n$ , in the cases where this value is lower than 50. These configurations were randomly generated (more about this generation in section 3.1

- Equivalent  $k_{\text{eff}}$  among configurations having the same number of MFR  $n$  and the same contact surfaces, with a variability of 250 pcm,
- The most reactive configurations are the ones of greater  $s$ .

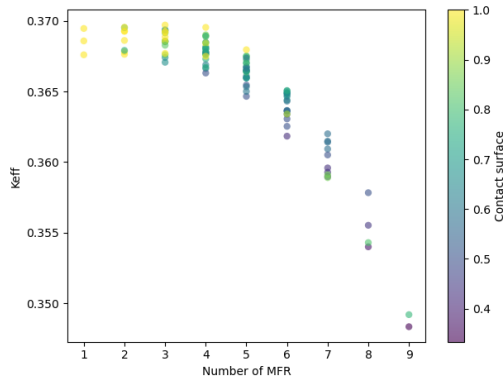


Figure 33.  $k_{\text{eff}}$  for the  $5 \times 5$  isolated configurations.

The permission to increase the value of  $s$  by adding MFR in periphery was not correlated with an increase in reactivity. This could be due to a smaller impact of the additional moderation provided by the MFR in the periphery, since the fuel rods there are already well moderated by the surrounding water. This would be in line with the previous assumption of no MFR in periphery.

#### 4.1.2 Study Case 2: $17 \times 17$ Assembly

The results for the random and MH generations are now presented.

##### Random generation

Figure 34 presents the results of  $k_{\text{eff}}$  for the random generation of Figure 24. The maximum value of  $k_{\text{eff}}$  is found for  $n=60$ . A typical pattern of 35 MFR, often used as reference, is included. As expected, results do not form an upper-bound curve for  $k_{\text{eff}}$ , since  $k_{\text{eff}}$  of the reference pattern is 800 pcm above the curve.

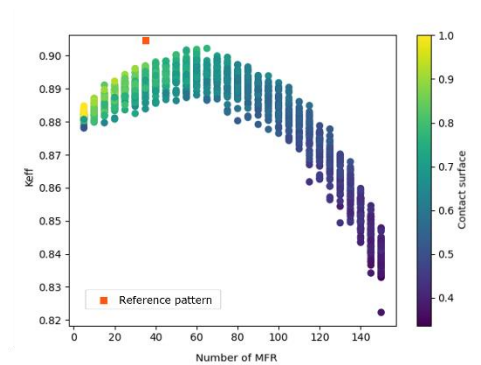


Figure 34.  $k_{\text{eff}}$  for the  $17 \times 17$  isolated assembly, random generation (1470 cases).

In conclusion, the results from the random generation are not representative, which supports the use of MH method for further generations.

### MH generation

The results of the configurations generated are presented in Figure 35, where we can see the equivalence of  $k_{\text{eff}}$  for same  $n$  and  $s$  already perceived in the  $5 \times 5$  assembly.

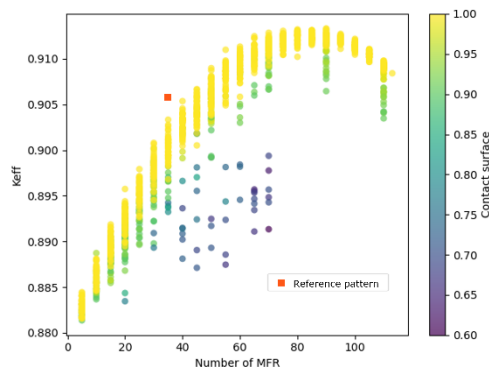


Figure 35.  $k_{\text{eff}}$  results for the  $17 \times 17$  isolated assembly, MH generation.

With respects to the random generation, MH finds a much higher value of  $k_{\text{eff}}^{\text{max}}$  (1000 pcm above) and shifted from  $n=60$  to  $n=90$ . For  $n=35$ ,  $k_{\text{eff}}$  of the reference pattern is still above the curve but only by 200 pcm.

The last results from MH aim at the study of the residual variation phenomena. In Figure 36 the grouping of  $k_{\text{eff}}$  for same  $(n, s)$  can be seen, along with the existence of the residual

variation. To quantify this variation, the standard deviation of the each  $(n, s)$  sample is calculated (Figure 37a). Similarly, the maximum difference of  $k_{\text{eff}}$  ( $\Delta k_{\text{eff}}^{\text{max}}$ ) within each  $(n, s)$  sample is plotted in Figure 37b.

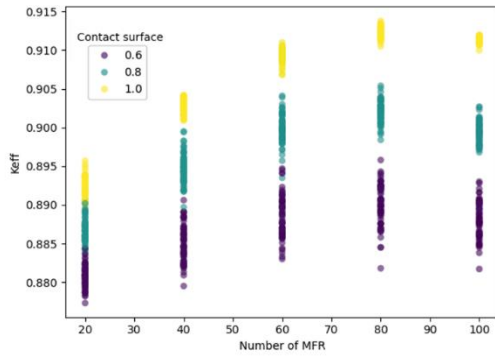


Figure 36.  $k_{\text{eff}}$  results for the  $17 \times 17$  isolated assembly. MH generation,  $s=0.6$ ,  $s=0.8$ ,  $s=1$ .

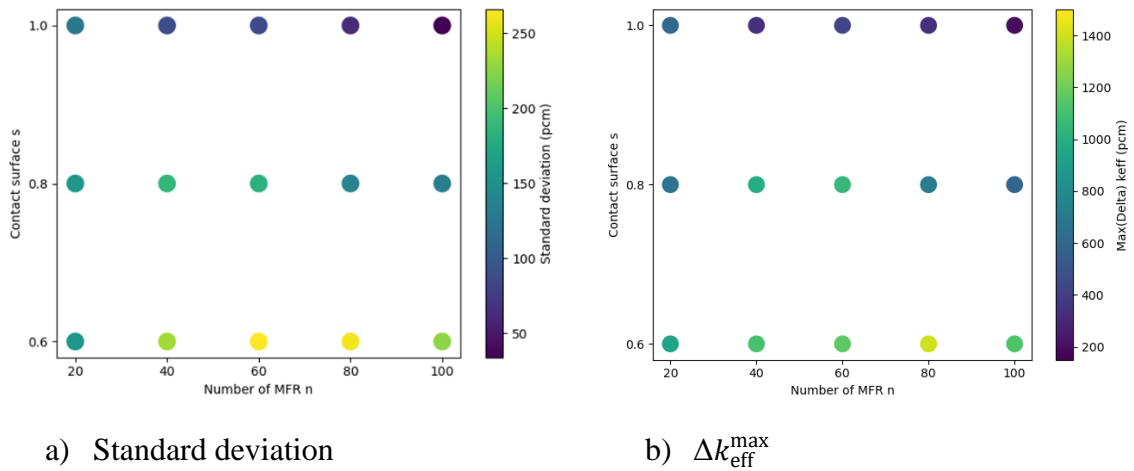


Figure 37. Dispersion of the samples in the  $(n, s)$  space,  $17 \times 17$  isolated assembly.

Standard deviations of the samples are limited to 250 pcm, however,  $\Delta k_{\text{eff}}^{\text{max}}$  reaches the 1400 pcm. The  $(n, s)$  pairs showing greater variability in  $k_{\text{eff}}$  are also the ones with lower contact surfaces and thus the ones, according to the method and to the results, that are not expected to have higher reactivities. For the high  $s$ , especially for high values of  $n$ , the results are less dispersed ( $\sigma < 50$  pcm).

## 4.2 Other Boundary Conditions: Is the Contact Surface Method Still Valid?

Results of  $k_{\text{eff}}$  for water-concrete boundary conditions and the array of assemblies are now presented in relation to contact surfaces.

### 4.2.1 Study Cases 3 and 4: Water-Concrete Boundary Conditions

#### Study case 3: 5×5 assembly

Results for the 5×5 assembly with no MFR in periphery in water-concrete conditions appear in Figure 38. Regarding the capacity of the contact surface to group configurations, no difference was perceived with respects to the isolated 5×5 assembly.

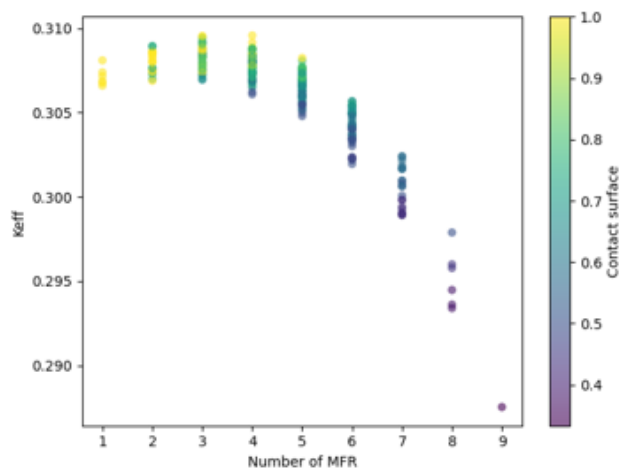


Figure 38.  $k_{\text{eff}}$  for the 5×5 assembly with no MFR in periphery, water-concrete.

#### Study case 4: 17×17 assembly

The results of the 17×17 water-concrete case are shown in Figure 39.

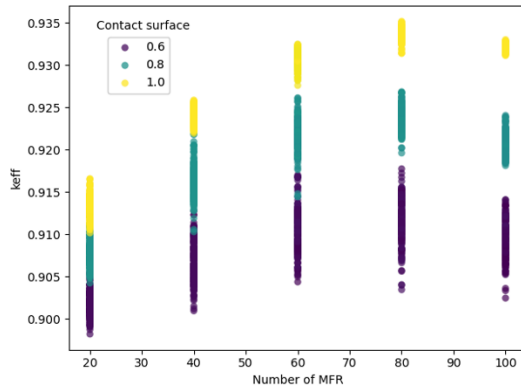
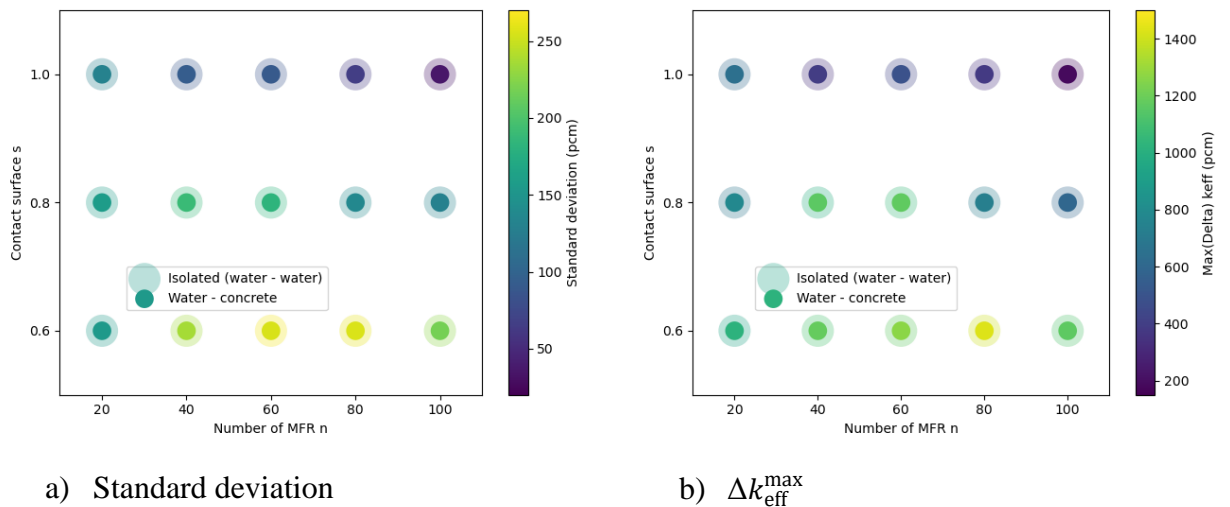


Figure 39.  $k_{\text{eff}}$  results for the  $17 \times 17$  assembly, water-concrete. MH generation,  $s=0.6$ ,  $s=0.8$ ,  $s=1$ .

Results of  $\sigma$  and  $\Delta k_{\text{eff}}^{\text{max}}$  are shown in Figure 40 compared with the results from the isolated assembly.



a) Standard deviation

b)  $\Delta k_{\text{eff}}^{\text{max}}$

Figure 40. Dispersion of the samples in the  $(n, s)$  space. Comparison of isolated and water water-concrete concrete conditions ( $17 \times 17$  assembly).

The conclusion is that no particularly higher dispersion is found for the water-concrete case, contrarily to what was expected.

### 4.2.2 Study Case 5: Array of Assemblies

The results of the array case for different distances are shown in Figure 41. The order of magnitude being quite dependant on the distance (the longer the distance between assemblies, the lower reactivity is) results are better visualised in Appendix 2, where they are separately presented for each distance. In any case, the tendency of higher  $k_{\text{eff}}$  for higher  $s$  is maintained. In addition, the residual variation of each case is studied with  $\sigma$  and  $\Delta k_{\text{eff}}^{\text{max}}$  (Figure 42 ).

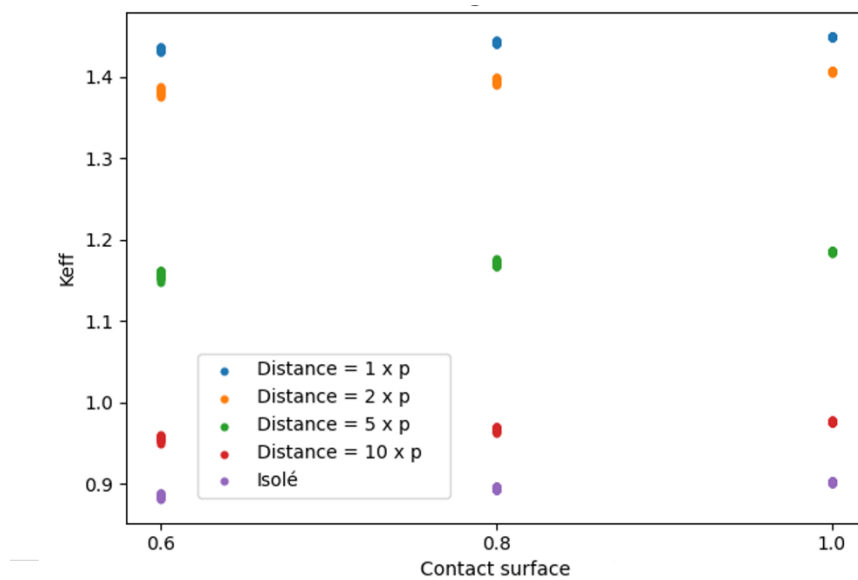
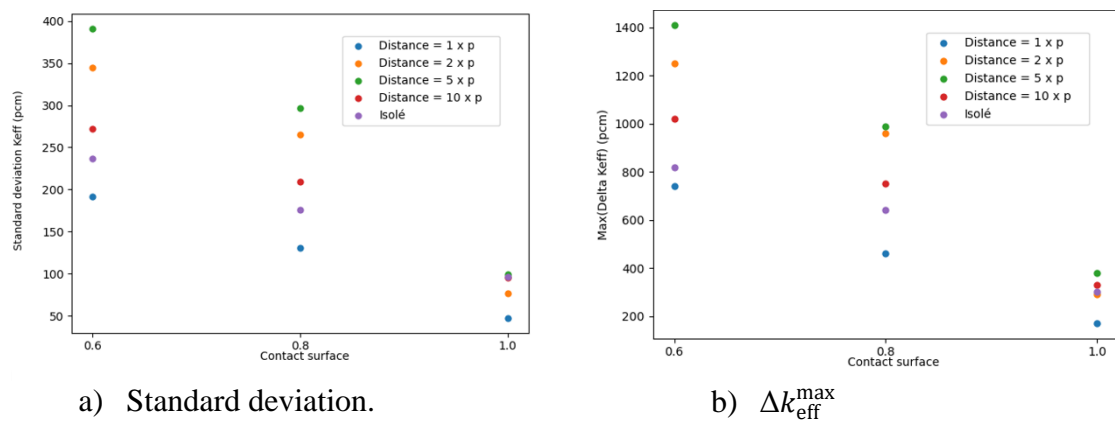


Figure 41.  $k_{\text{eff}}$  as a function of contact surface for the different distances between assemblies.



a) Standard deviation.

b)  $\Delta k_{\text{eff}}^{\text{max}}$

Figure 42. Dispersion of  $k_{\text{eff}}$  for the differences distance in the array of assemblies.

It can be concluded that the dispersion is higher for the array than for the isolated assembly, except when the distance is equal to the pitch. In that case, results are even more precise as the isolated assembly. In fact, this situation can be perceived like the case of an infinite assembly with a fixed pattern of MFR in the space between assemblies.

In Figure 43 the standard deviation  $\sigma$  for  $s=0.6$  is plotted as a function of the distance, to better visualise which distance gives the more disperse results, which is found to be 5 times the nominal pitch.

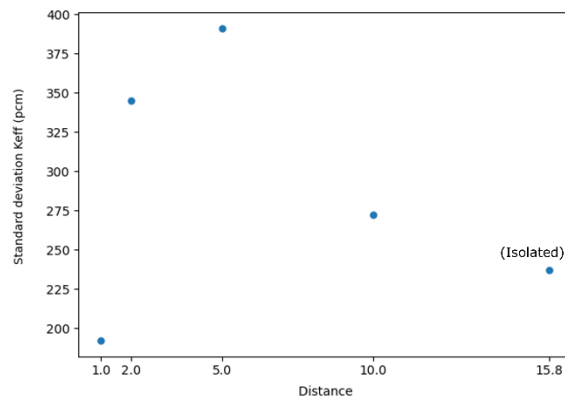


Figure 43. Standard deviation as a function of the distance (in terms of pitch),  $n=40$ ,  $s=0.6$ .

For this reason, the case  $n=40$ , distance= $5 \times$ pitch was studied in more detail. As shown in Figure 44,  $s=1$  still compounds the upper-bound curve of the results, which proves that the contact surface method remains pertinent.

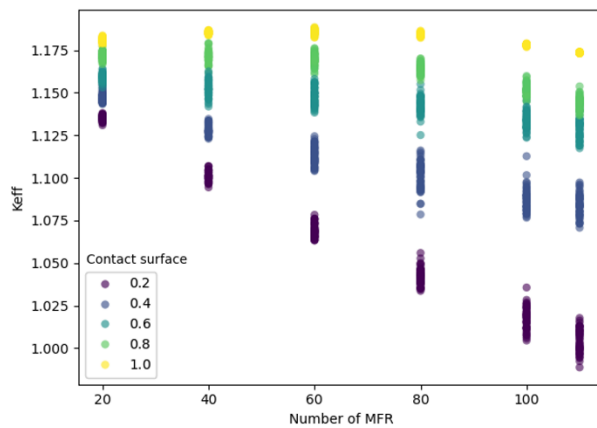
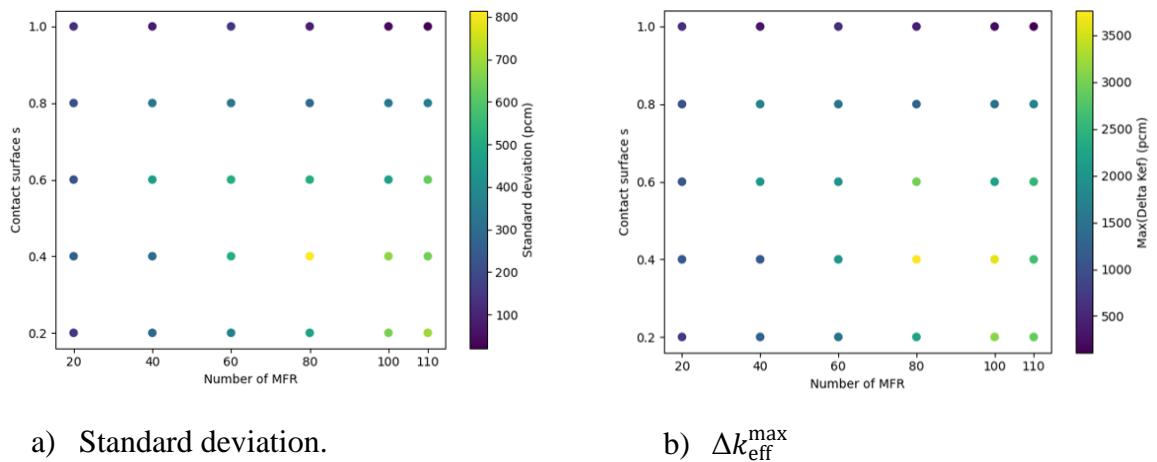


Figure 44.  $k_{\text{eff}}$  as a function of  $n$  and  $s$  for the array of assemblies, distance= $5 \times \text{pitch}$ .



a) Standard deviation.

b)  $\Delta k_{\text{eff}}^{\text{max}}$

Figure 45. Dispersion of the samples in the  $(n, s)$  space, array of assemblies with distance =  $5 \times \text{pitch}$ .

However, the residual variation is higher with respects to the isolated case (Figure 45). Standard deviation  $\sigma$  reaches the 500 pcm for  $s=0.6$ , while in the isolated case was limited to 250 pcm (Figure 37). The tendency of less dispersion for higher values of reactivity is maintained.

### 4.3 Comparison of Most Reactive Patterns: Contact Surface Method vs. Generational Genetic Algorithm

In this section, the configurations generated, as well as the reference configurations obtained by the gGA, present the characteristics of the study case 6.

#### 4.3.1 Results from Metropolis-Hastings

The results of  $k_{\text{eff}}$  for the first MH sample ( $0.8 < s < 1.0$ ) are displayed in Figure 46. It can be seen how the gGA was not able to find the most overall penalising case. Although  $k_{\text{eff}}^{\text{max}}$  (0.9854) found by MH is 400 pcm above  $k_{\text{eff}}^{\text{CEA}}$  and is indeed found for  $s=1$ , Figure 46 seems to be showing some limitation of the MH algorithm. In fact, for  $s \approx 0.84$ , the configurations found by MH are considerably less reactive than the CEA pattern.

This is why a deeper study of configurations in the region of  $s_{\text{CEA}}$  was done. Figure 47 shows the results of  $k_{\text{eff}}$  for the second MH sample.

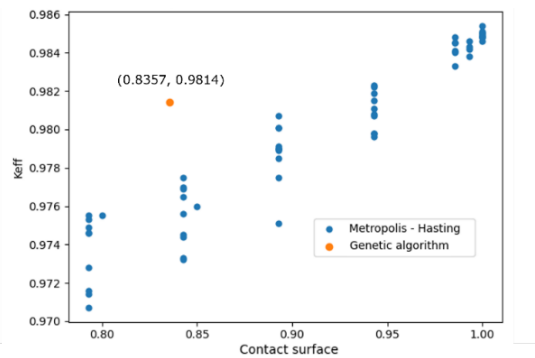


Figure 46.  $k_{\text{eff}}$  for the  $16 \times 16$  assembly, comparison MH generation and CEA result.

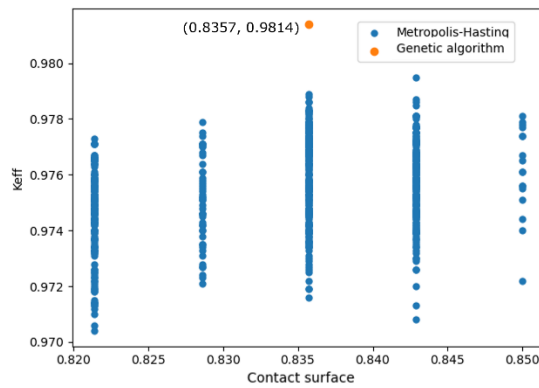


Figure 47.  $k_{eff}$  for the  $16 \times 16$  assembly, comparison MH generation for  $s$  around  $s_{CEA}$  and CEA result.

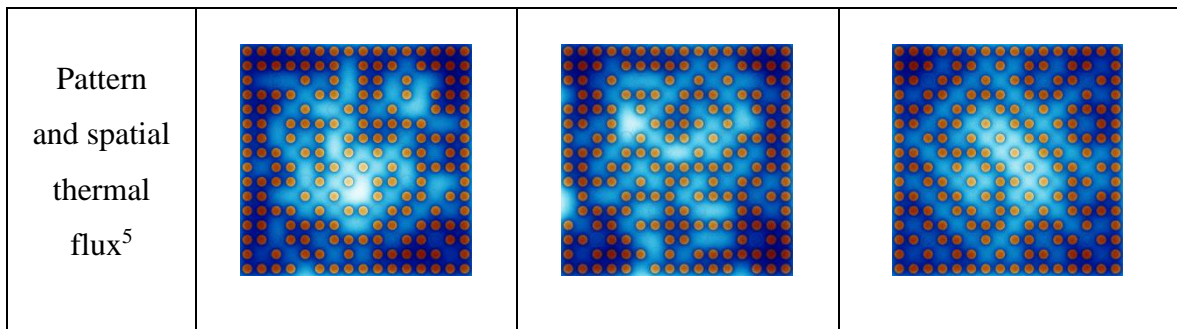
The difference in  $k_{eff}$  was reduced to 250 pcm, but  $k_{eff}^{CEA}$  remained clearly above the rest of the sample, so further efforts had to be put in this direction, as described in the next sections.

#### 4.3.2 Thermal Flux

To get a deeper insight of the phenomena, the patterns of the configurations were observed along with their spatial thermal flux (Table 3).

Table 3. Patterns of the configurations of the  $16 \times 16$  assembly to study in detail.

	(A)	(B)	(C)
Description	CEA pattern	MH pattern with $s=s_{CEA}$ and maximum $k_{eff}$	MH pattern with absolute maximum $k_{eff}$
$s$	0.8357	0.8357	1
$k_{eff}$	0.9814	0.9789	0.9854



The major remarks are:

- The gGA avoided the MFR in periphery,
- The gGA found a configuration with particularly high thermal flux in the centre of the assembly,
- MH searching for  $s=1$  will find configurations with no MFR in periphery by definition, however, for  $s<1$ , MFR are allocated also in the periphery. This may be the cause of the inferiority of  $k_{\text{eff}}$  found by MH compared to gGA.

On this basis, the imposition of no MFR in the periphery was chosen. The results are this time presented in the histogram of Figure 48.

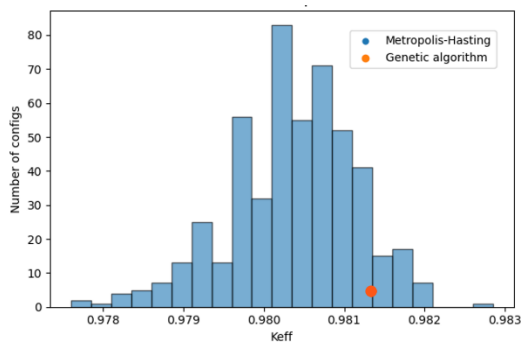


Figure 48. Histogram of  $k_{\text{eff}}$  for 500 configurations generated by MH with no MFR in periphery,  $n=50$ ,  $s=s_{\text{CEA}}$ .

<sup>5</sup> The orange colour indicates relative fission power, and blue colour, the thermal flux. Darker colours indicate lower values and lighter colours indicate higher values.

Although the distribution is centred in a value of  $k_{\text{eff}}$  lower than  $k_{\text{eff}}^{\text{CEA}}$ , this time the distribution includes  $k_{\text{eff}}^{\text{CEA}}$  and some configurations even have  $k_{\text{eff}} > k_{\text{eff}}^{\text{CEA}}$ . As a general conclusion, the results indicate that the MH algorithm on its own may not be the most efficient method to find the most reactive configurations. In some cases, it should be tuned with constraints like the one used in the previous results to avoid MFR in periphery.

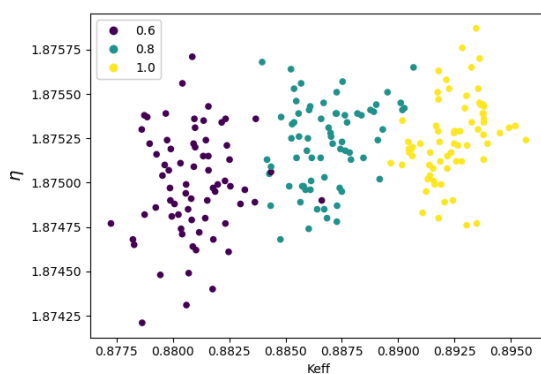
#### 4.4 Attempts to Refine the Contact Surface Parameter: Results

Several variables and new studies were done to observe the behavior of the incomplete assemblies.

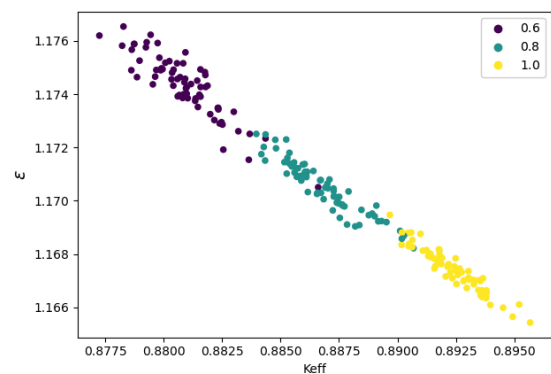
##### 4.4.1 Six-Factor Formula

The following results will attempt to use the six-factor formula to explain the relation higher  $s$ –higher  $k_{\text{eff}}$ , and the dispersion of  $k_{\text{eff}}$  for a  $(n, s)$  pair.

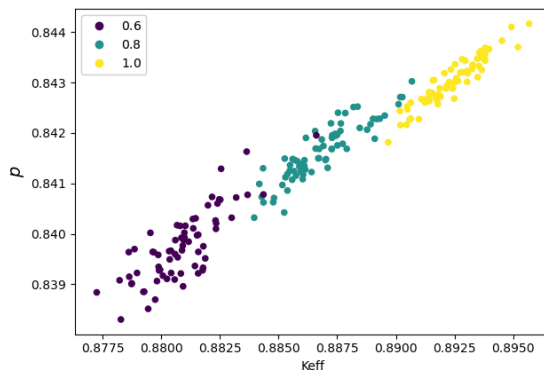
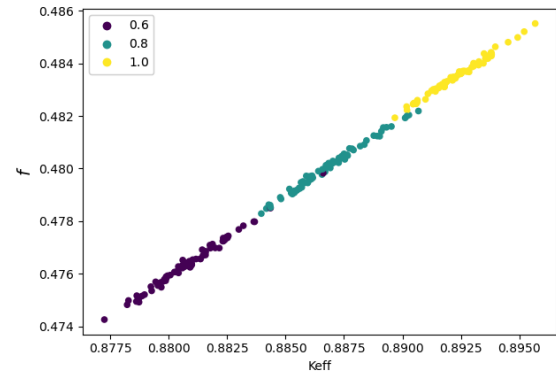
For the isolated  $17 \times 17$  assembly, Figure 49 shows the four factors for the 210 configurations run for  $n = 20$ , as a function of their  $k_{\text{eff}}$  and grouped by their contact surface.



a) Thermal fission factor  $\eta$

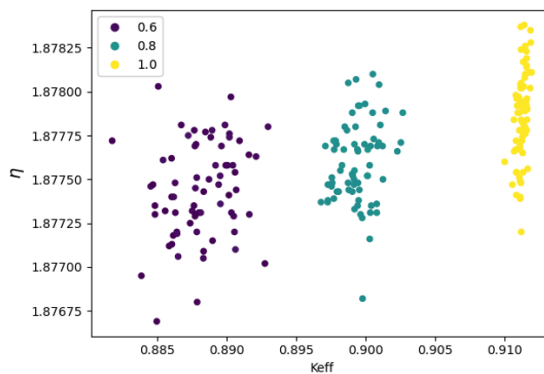
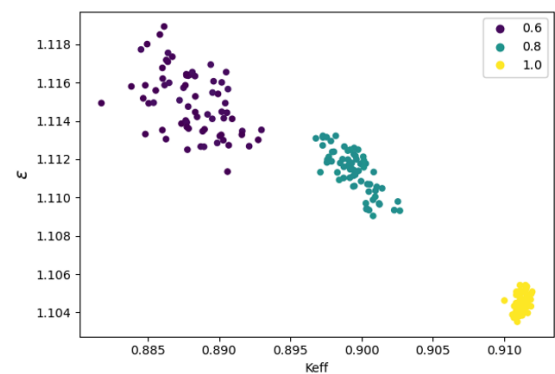


b) Fast fission factor  $\epsilon$

c) Resonance escape probability  $p$ d) Thermal utilization factor  $f$ Figure 49. Four factors for  $n=20$ .

Only the fast fission factor has a decreasing contribution to  $k_{\text{eff}}$  as  $s$  increases, but the other three factors compensate for that and allow the well-known relation higher  $s$ -higher  $k_{\text{eff}}$ . The thermal fission factor  $\eta$  has a poor impact, while the resonance escape probability  $p$ , and especially the thermal utilization factor  $f$ , have the biggest influence in the increase of reactivity. In fact, these are the factors representing the efficiency of moderation.

To have a first insight on the contribution of these factors to the residual variation, Figure 50 presents the same graphs but for  $n=100$ , where the residual variation of  $k_{\text{eff}}$  is particularly low for  $s=1$ . For 100 MFR, the four factors follow the same trends that for 20 MFR. The factors  $\varepsilon$ ,  $p$  and  $f$  get more concentrated as  $s$  increases, explaining the reduction of the residual variation.

a) Thermal fission factor  $\eta$ b) Fast fission factor  $\varepsilon$

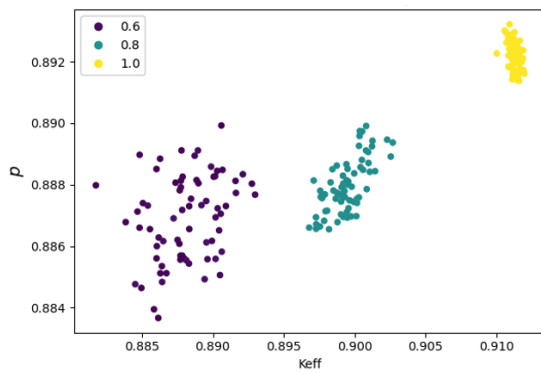
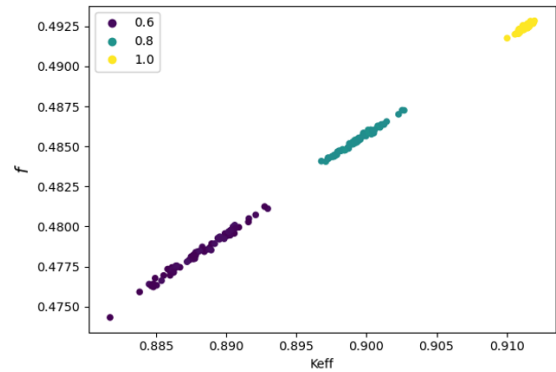
c) Resonance escape probability  $p$ d) Thermal utilization factor  $f$ Figure 50. Four factors for  $n=100$ .

Figure 51 presents the dispersion of each factor in terms of the standard deviation and for the whole  $(n, s)$  space studied. The thermal fission factor  $\eta$  has a small impact on  $\sigma$ , and it remains constant in the whole space. Consequently,  $p$  and  $f$  are of particular interest to understand the evolution of  $\sigma_{keff}$  in the  $(n, s)$  space.

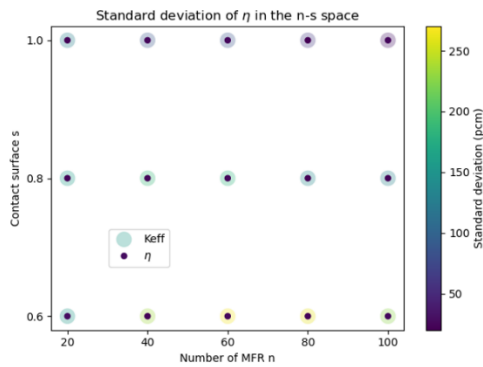
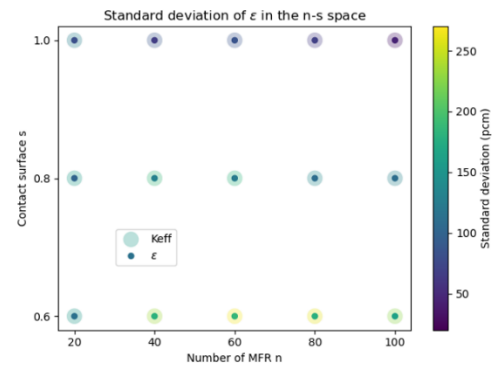
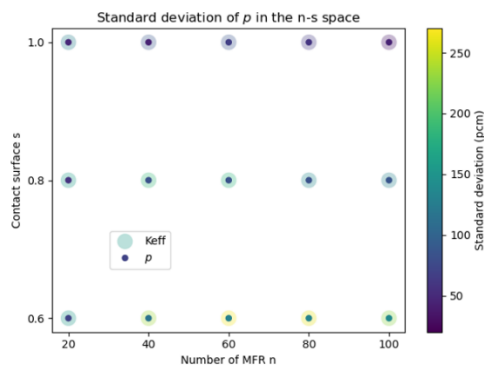
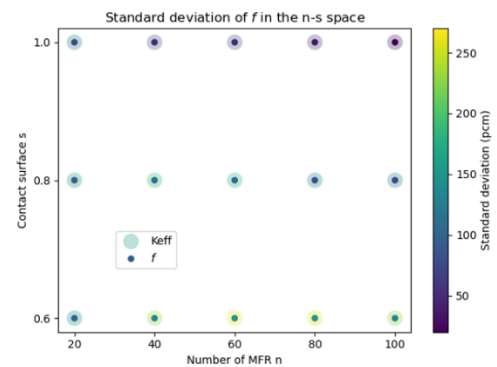
a) Thermal fission factor  $\eta$ b) Fast fission factor  $\epsilon$ c) Resonance escape probability  $p$ d) Thermal utilization factor  $f$

Figure 51. Standard deviation of each factor in the n-s space, compared to the standard deviation of  $k_{\text{eff}}$ .

Results of the four-factor formula were also obtained for study case 6. Figure 52 includes all the cases of study case 6 with  $s = s_{\text{CEA}}$ , including the ones with no MFR in periphery.

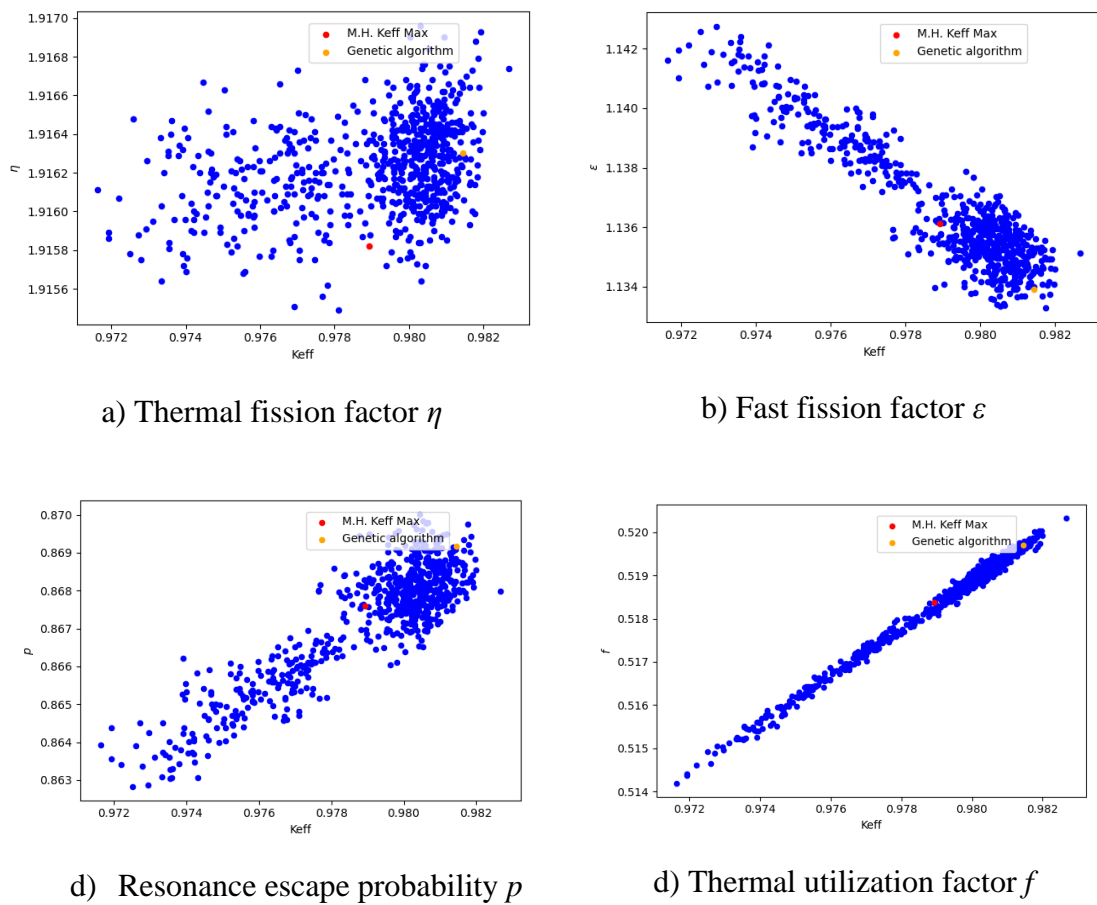


Figure 52. Four-factor formula results for the study case 6<sup>6</sup>.

The red point indicates configuration (B) in Table 3, that is, the MH case with  $k_{\text{eff}}^{\text{max}}$  but MFR in periphery; the orange one, configuration (A) in Table 3 (CEA pattern). Again, it is owing to factors  $p$  and  $f$  that the configuration found by the gGA is more reactive.

<sup>6</sup> The points in blue are all the cases calculated in section 3.4.3

#### 4.4.2 Detectors

Reaction rates (fission, elastic scattering, and absorption) in the assembly and in the fuel for the three configurations in Table 3 are shown in Figure 53.

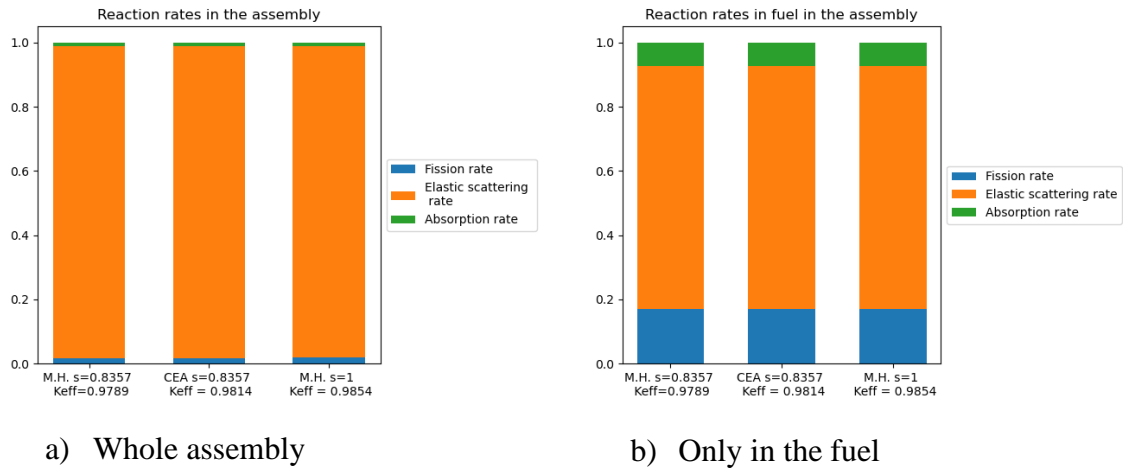


Figure 53. Reaction rates in the three configurations in Table 3.

No differences can be seen, so the solution passes by testing other parameters. For instance, the ratio losses to total thermal flux and the ratio captures in water to captures in fuel are displayed in Figure 54. Surprisingly, the leakage is higher for the most reactive case where, on the contrary, the captures in water are fewer.

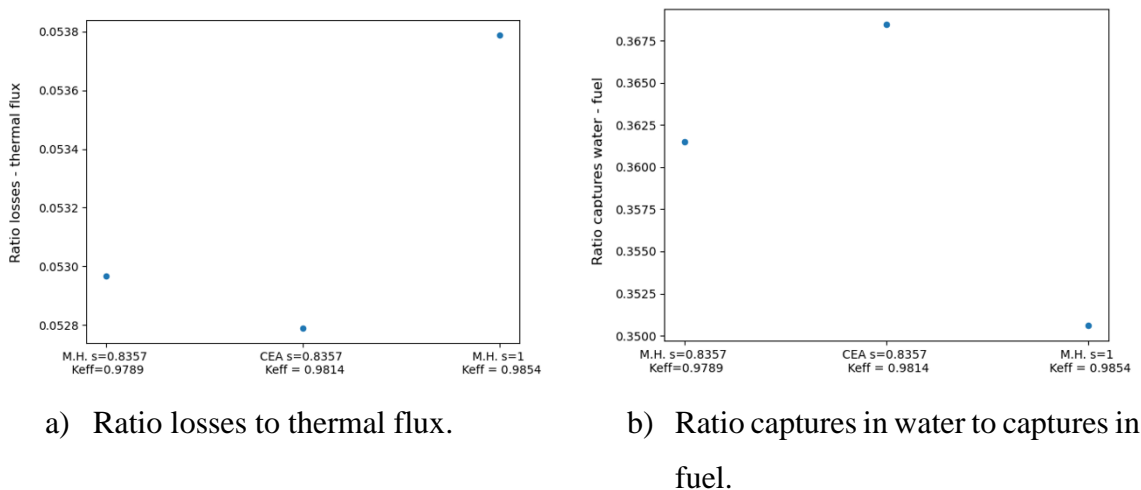


Figure 54. Ratios of magnitudes from detectors for the configurations in Table 3.

The thermal flux profiles of the configurations (Figure 55a) differ in the inner rings, being the flux higher for the configuration found by the gGA. In the three cases, capture and fission rates find their maximum in ring 8 of the assembly, while elastic scattering diminishes (Figure 56). This indicates that neutrons, either by the influence of the surrounding water or by the inner part of the assembly, are well thermalised in this partition. The main difference in the distributions of the three configurations is how the  $s=1$  case presents a smoother profile of all the reaction rates.

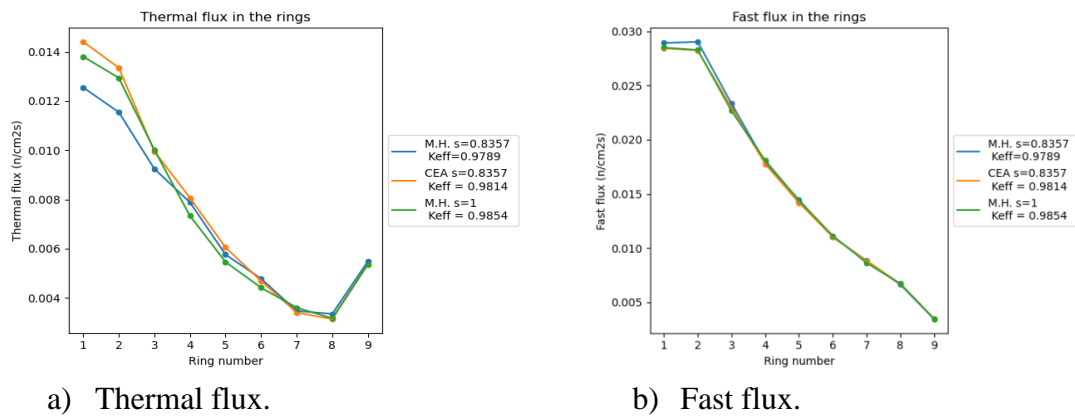


Figure 55. Flux by ring in the assembly for the configurations in Table 3.

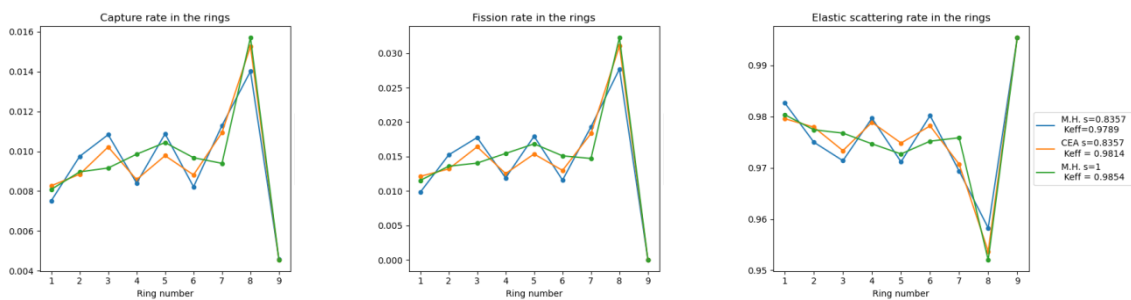
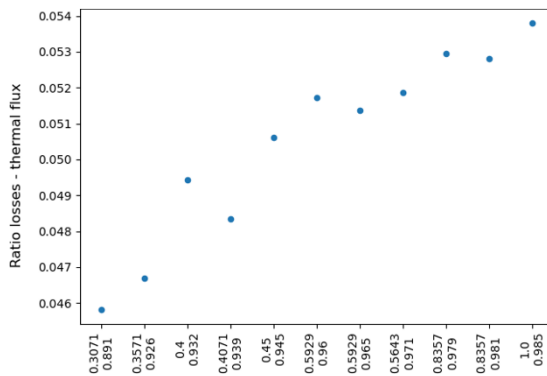


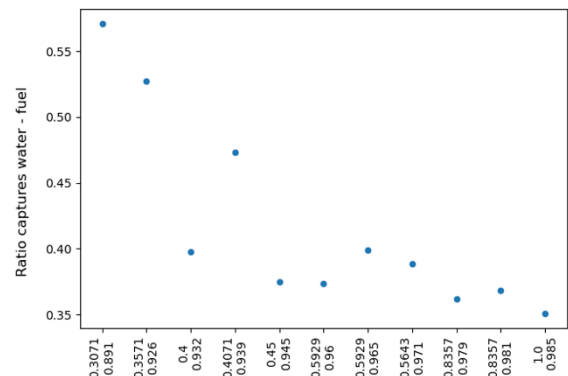
Figure 56. Reaction rates by ring in the assembly for the configurations in Table 3.

As a general conclusion, it can be said that it is difficult to compare the configurations in Table 3 with the information recovered by the detectors. These configurations are already very similar, so the parameters explaining their difference in reactivity may require a finer analysis. To test the pertinence of the detectors, new configurations of study case 6 were studied, this time having lower values of  $s$ .

The ratios losses to total thermal flux and the ratio captures in water to captures in fuel for each configuration are presented in Figure 57. The labels of the x axis represent the  $s$  and  $k_{\text{eff}}$  of each configuration, from lower to higher. The ratio losses to total thermal flux increase for more reactive configurations, while the ratio captures in water to captures in fuel decreases.



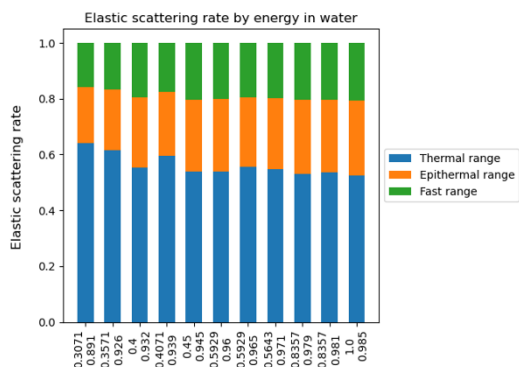
a) Ratio losses to thermal flux.



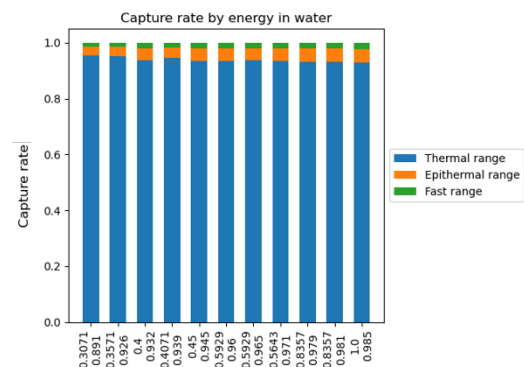
b) Ratio captures in water to captures in fuel.

Figure 57. Ratios of magnitudes from detectors, configurations of study case 6 with different values of  $s$ .

To observe the process of thermalisation in the different configurations, elastic scattering and capture rates by energy of the neutron are displayed in Figure 58. The reactions measured are the ones taking place in the water inside the assembly.



a) Elastic scattering rate.



b) Capture rate.

Figure 58. Elastic scattering and capture rates by energy of the neutron in water within the assembly.

As  $k_{\text{eff}}$  increases, a higher proportion of the elastic scatterings take place in the fast and epithermal range, and a smaller proportion of captures in the thermal range. These trends are in line with a more efficient thermalisation of the neutrons leading to higher reactivities.

#### 4.4.3 Fission Matrix

The fission matrices of each pattern of Figure 29 are presented in Figure 59, along with their  $k_{\text{eff}}$ . The colours (lighter for higher values, darker for lower) represent the number of neutrons normalised by the surface of the region.

The first result to remark is how the inner configuration presents the maximum  $k_{\text{eff}}$ . It is 170 and 770 pcm higher than the medium and outer configurations, respectively. The (2, 2) element of the matrix for the inner case presents remarkably higher values than for the others: the neutrons born in the periphery produce more fissions in the periphery too, despite not having the presence of additional moderation of MFR. This supports the previously expressed idea that the moderation provided by the surrounding water is efficient enough, and that the maximization of fuel in the periphery optimises reactivity.

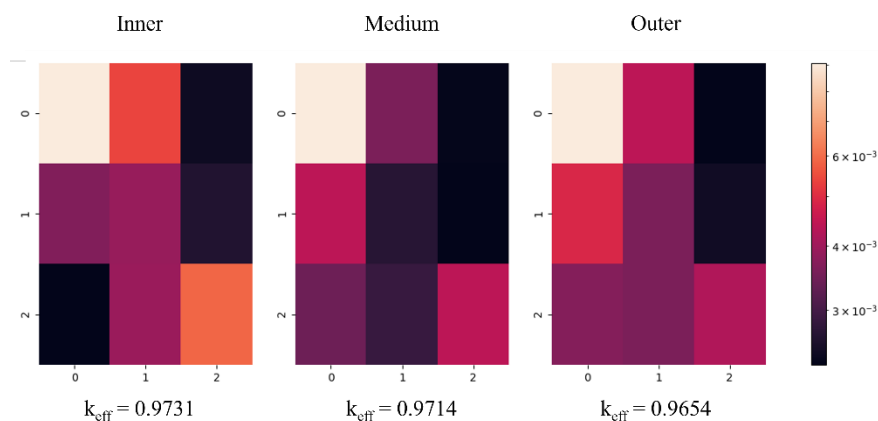


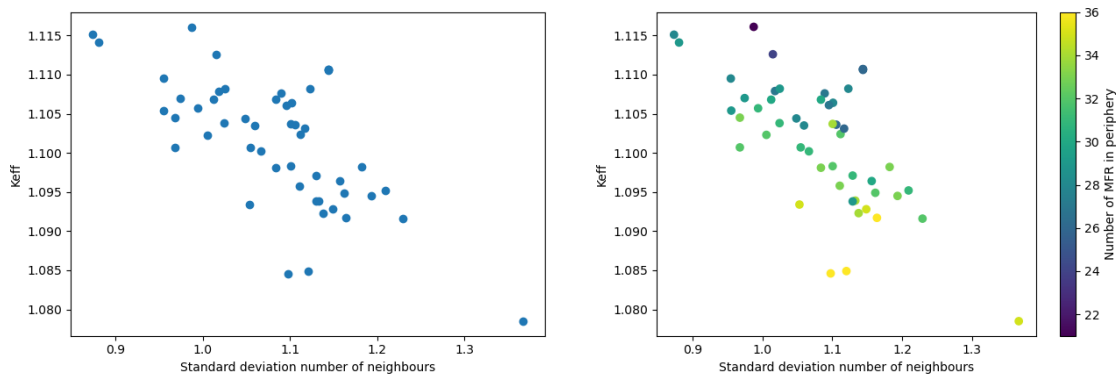
Figure 59. Fission matrix of the inner, medium and outer configurations.

As a general conclusion, no evidence on how the fission matrix should be to have more reactive configuration was found. A more thorough analyses could link fission matrix and perturbation theory to study the effect of the replacement of one fuel pin by a MFR.

#### 4.4.4 Dispersion of the contact surface within the assembly

The results for the variable “standard deviation of  $s$ ” ( $\sigma_s$ ), described in section 3.5.1 are now presented.

Figure 60a shows  $k_{\text{eff}}$  as a function of  $\sigma_s$  for the assembly in the array with distance =  $5 \times \text{pitch}$ ,  $n=80$ ,  $s=0.4$  (50 configurations). The figure suggests a certain relation between a lower  $\sigma_s$  and greater  $k_{\text{eff}}$ . Due to the intuition emerging from previous results that MFR in the periphery have an effect on the reactivity, the number of MFR in periphery is also displayed in Figure 60b. A bigger value of the number of MFR groups less reactive configurations.

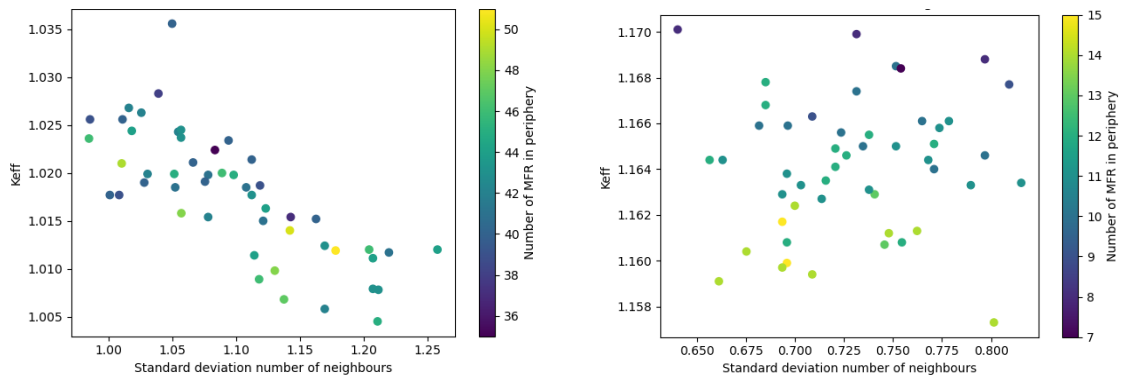
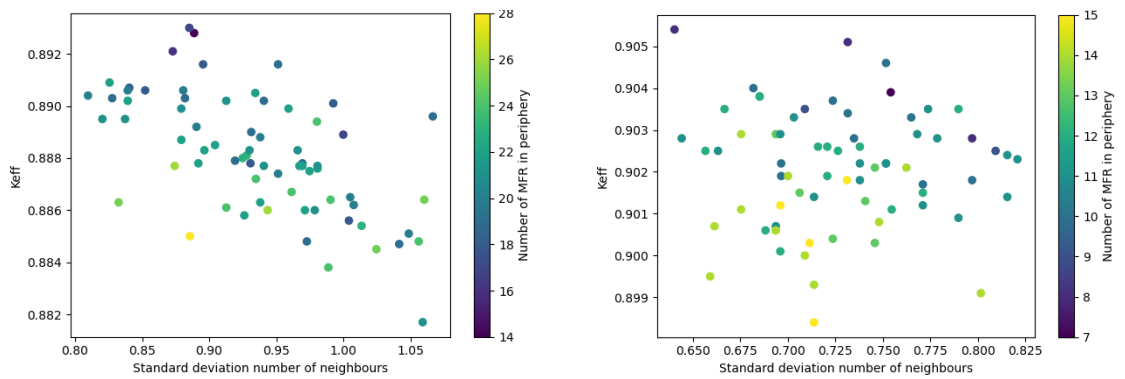


a)  $k_{\text{eff}}$  as a function of  $\sigma_s$

b)  $k_{\text{eff}}$  as a function of  $\sigma_s$ , colored according to the number of MFR in periphery.

Figure 60.  $k_{\text{eff}}$  as a function of  $\sigma_s$ , results for the array of assemblies, distance =  $5 \times \text{pitch}$ ,  $n=80$ ,  $s=0.4$  (50 configurations).

After these first results, the same plots are done for other points of the  $(n, s)$  space. The relation here becomes much more ambiguous, as can be seen in examples of Figure 61. When applied to the isolated  $17 \times 17$  assembly, the variable is meaningless for a huge portion of the  $(n, s)$  space (Figure 62).

a)  $n = 100, s=0.6$ , 50 configurations.b)  $n = 80, s=0.8$ , 50 configurations.Figure 61.  $k_{\text{eff}}$  as a function of  $\sigma_s$ , results for the array of assemblies, distance =  $5 \times \text{pitch}$ .a)  $n = 100, s=0.2$ , 70 configurations.b)  $n = 80, s=0.8$ , 70 configurations.Figure 62.  $k_{\text{eff}}$  as a function of  $\sigma_s$  in the isolated  $17 \times 17$  assembly.

For  $s = 1$ ,  $\sigma_s = 0$  since all MFR are invariably surrounded by 4 fuel rods. The samples with  $s=1$  are also the ones with less dispersion of  $k_{\text{eff}}$  so in that sense, the use of the standard deviation of  $s$  as a complementary magnitude to  $s$  seems to be pointing in the right direction. Moreover, the variable works better for lower  $s$ , where the greatest  $k_{\text{eff}}$  dispersion is found. However, in the light of the previous results,  $\sigma_s$  is a very case-sensitive parameter: it is pertinent depending on the point of the  $(n, s)$  space. Further improvement in its definition (for instance, to better model the presence of MFR in the periphery) may lead to more conclusive results.

## 5 Conclusions

The modelling of incomplete assemblies (assemblies from which an arbitrary number of fuel rods have been removed) for the criticality-safety analyses is a challenging problem. The presence of Missing Fuel Rods (MFR) at the storage level may increase  $k_{\text{eff}}$ , not only depending on the number of MFR but also on their positions. The impossibility to model all the possible patterns has led to different methods being proposed.

The contact surface method proposes a geometrical variable  $s$  of the MFR patterns that would complement the number of MFR  $n$  so that the couple  $(n, s)$  would be able to fully parametrise the  $k_{\text{eff}}$ . To pave the  $(n, s)$  space, the Metropolis-Hasting algorithm has been put in place. The capability of MH to find rare, and also more reactive, configurations has been proved.

The method has been validated for the isolated case, although some dispersion in  $k_{\text{eff}}$  was still found in the  $(n, s)$  samples. When applied to new boundary conditions like the water-concrete case no greater dispersion of the results was perceived, contrarily to what was expected. The array case presented higher dispersion, but the method still seems pertinent.

By means of Metropolis-Hasting algorithm, configurations of high values of  $s$  were generated, having greater reactivity than the patterns found by generational Genetics Algorithms. However, for lower values of  $s$ , the gGA was able to find patterns with higher  $k_{\text{eff}}$  than MH.

Further work to treat the issue of MFR and the contact surface method can be done. On one hand, more efforts can be done to explain some of the phenomena found, such as the effect of water-concrete boundary conditions in the incomplete assemblies. Some preliminary results of the effect of water-concrete have been presented, but they must be continued. The effect of the distance between assemblies in the array case can lead to future studies too. On the other hand, new parameters or approaches can be explored to complement and improve the contact surface method and reduce the dispersion of  $k_{\text{eff}}$  in the  $(n, s)$  samples. This is the case of the exploration of the fission matrix as a useful tool for the treatment of the problem.

## References

- Albert, T. et al. 2019. *An alternative simple approach for the modelling of fuel assemblies with missing fuel rod*. ICNC 2019 - 11th International conference on Nuclear Criticality Safety.
- Carney, S. et al. 2013. *Fission Matrix Capability for MCNP, Part II – Applications* - International Conference on Mathematics and Computational Methods Applied to Nuclear Science & Engineering (M&C 2013).
- Dechenaux, B., Delcambre, T. & Malvagi, F. 2023. Criticality safety of fuel assemblies with missing fuel rods. (Preprint Annal of Nuclear Energy).
- Duderstadt, J.J., Hamilton, L. J. (1977) *Nuclear Reactor Analysis*.
- Dupas, J. (2023). *Missing rods pattern optimization in LWR fuel assembly using a genetic algorithm coupled with heterogeneous tripoli-4® Monte Carlo code calculations*. ICNC 2023 – The 12th International Conference on Nuclear Criticality Safety.
- Duquenne, S. et al. 2023. *Criticality calculations of spent fuel storage pool with water holes*. ICNC 2023 – The 12th International Conference on Nuclear Criticality Safety.
- Henry, A. 1975. *Nuclear Reactor Analyses*. MIT Press, Cambridge, Mass.
- Hoefer, A. et al. 2019. *Homogenisation techniques for bounding criticality safety analyses for fuel fabrication and repair*. ICNC 2019 – The 11th International conference on Nuclear Criticality Safety.
- IRSN (2024). Validation of the criticality safety CRISTAL V2 package on ICSBEP benchmarks. Report IRSN 2024-00100.
- Leppänen, J., et al. (2015) "The SERPENT Monte Carlo code: Status, development and applications in 2013." *Annal of Nuclear Energy*, 82 (2015), pp. 142-150.
- OECD/NEA Data Bank (2024). JANIS web. Available at: <https://www.oecd-nea.org/janisweb/tree/N>

Rau, A., Walters, W. (2019) 'Applications of SERPENT's Fission Matrix Capability' [PowerPoint presentation]. SERPENT User's Group Meeting, Atlanta. Available at: [Fission Matrix Methods for Nuclear Thermal Propulsion Systems \(vtt.fi\)](#)

Reuss, P. 2008. Neutron Physics. Nuclear engineering, EDP Sciences.

Règle Fondamentale de Sûreté (RFS) I.3.c de l'ASN.

Taboga, M. (2021). *Metropolis-Hastings algorithm*, Lectures on probability theory and mathematical statistics. Kindle Direct Publishing. Available at: <https://www.statlect.com/fundamentals-of-statistics/Metropolis-Hastings-algorithm>.

The SERPENTTools developer team (2017-2019). *SERPENTTools*. Available at: [Publications — SERPENTTools documentation \(SERPENT-tools.readthedocs.io\)](#)

## Appendix

### Appendix 1. Study cases.

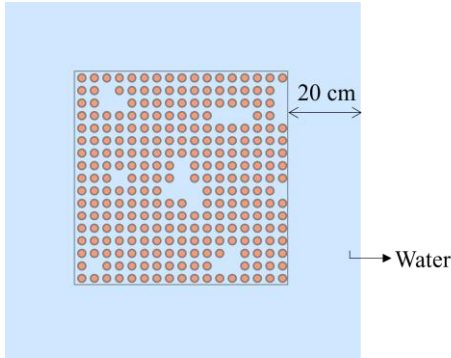


Figure 63. Scheme of the  $17 \times 17$  isolated assembly. For a better visualisation, water thickness in the picture is not scaled to its value.

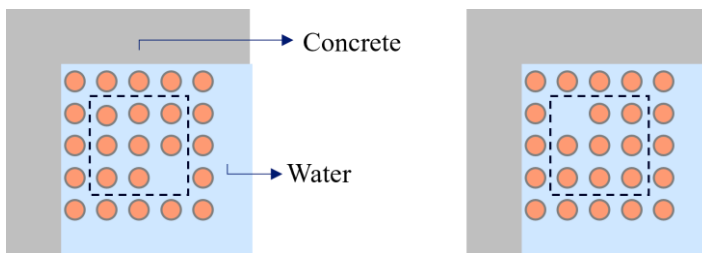


Figure 64. Example of two  $5 \times 5$  configurations that are no longer neutronically equivalent after the change in the environment.

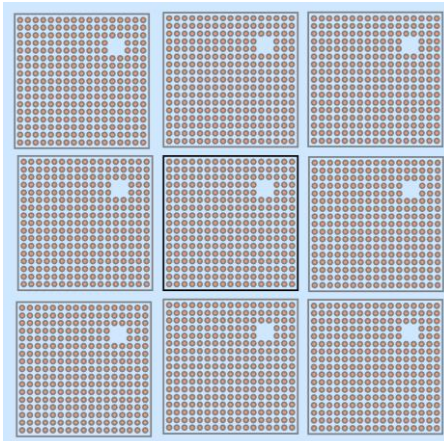
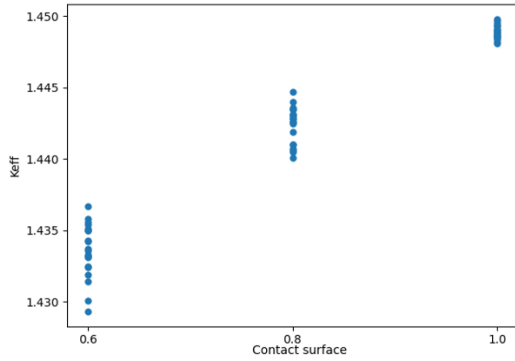
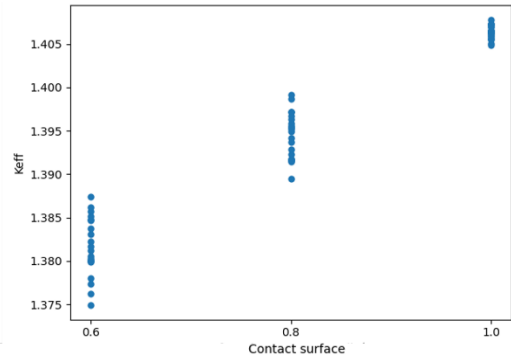


Figure 65. Scheme of the periodic boundary conditions applied to the assembly to simulate an array of assemblies.

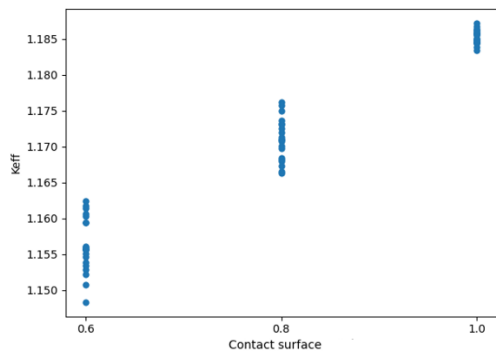
Appendix 2. Results of the array for different distances between assemblies.



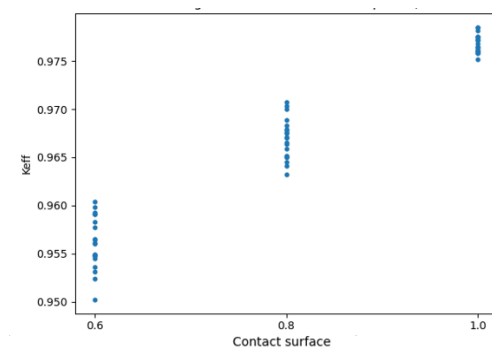
e) Distance =  $1 \times \text{pitch}$



f) Distance =  $2 \times \text{pitch}$



g) Distance =  $5 \times \text{pitch}$



h) Distance =  $10 \times \text{pitch}$

Figure 66.  $k_{\text{eff}}$  as a function of  $s$ .

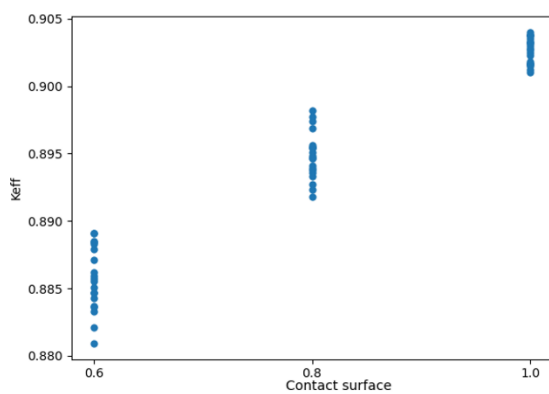


Figure 67.  $k_{\text{eff}}$  as a function of  $s$  for the isolated case.